Monthly Notices
of the
ROYAL ASTRONOMICAL SOCIETY

MNRAS **449,** 2087–2111 (2015) doi:10.1093/mnras/stv270

Four phases of angular-momentum buildup in high-z galaxies: from cosmic-web streams through an extended ring to disc and bulge

Mark Danovich,[1]★ Avishai Dekel,[1] Oliver Hahn,[2] Daniel Ceverino[3] and Joel Primack[4]

[1]*Center for Astrophysics and Planetary Science, Racah Institute of Physics, The Hebrew University, Jerusalem 91904, Israel*
[2]*Institute for Astronomy, Department of Physics, ETH Zürich, CH-8093 Zurich, Switzerland*
[3]*Departamento de Fisica Teorica, Universidad Autonoma de Madrid, Madrid E-28049, Spain*
[4]*Department of Physics, University of California, Santa Cruz, CA 95064, USA*

Accepted 2015 February 9. Received 2014 December 18; in original form 2014 July 25

ABSTRACT

We study the angular-momentum (AM) buildup in high-z massive galaxies using high-resolution cosmological simulations. The AM originates in co-planar streams of cold gas and merging galaxies tracing cosmic-web filaments, and it undergoes four phases of evolution. (I) Outside the halo virial radius ($R_{\rm v} \sim 100$ kpc), the elongated streams gain AM by tidal torques with a specific AM (sAM) $\sim$1.7 times the dark matter (DM) spin due to the gas' higher quadrupole moment. This AM is expressed as stream impact parameters, from $\sim 0.3R_{\rm v}$ to counter rotation. (II) In the outer halo, while the incoming DM mixes with the existing halo of lower sAM to a spin $\lambda_{\rm dm} \sim 0.04$, the cold streams transport the AM to the inner halo such that their spin in the halo is $\sim 3\lambda_{\rm dm}$. (III) Near pericentre, the streams dissipate into an irregular rotating ring extending to $\sim 0.3R_{\rm v}$ and tilted relative to the inner disc. Torques exerted partly by the disc make the ring gas lose AM, spiral in, and settle into the disc within one orbit. The ring is observable with 30 per cent probability as a damped Lyman α absorber. (IV) Within the disc, $<0.1R_{\rm v}$, torques associated with violent disc instability drive AM out and baryons into a central bulge, while outflows remove low-spin gas, introducing certain sensitivity to feedback strength. Despite the different AM histories of gas and DM, the disc spin is comparable to the DM-halo spin. Counter rotation can strongly affect disc evolution.

Key words: galaxies: evolution – galaxies: formation – galaxies: kinematics and dynamics – galaxies: spiral.

1 INTRODUCTION

The acquisition of angular momentum (AM) by galaxies is of fundamental importance for the understanding of galaxy properties and evolution. Being supported by rotation, the size, structure and dynamics of galactic discs, as well as the star formation in them, are predominantly determined by their AM and its distribution. In turn, the formation of spheroids is driven by AM losses.

The basic understanding of the origin of AM in galaxies is that, as the proto-galactic density perturbations grow, they acquire AM through the gravitational tidal torques exerted by neighbouring perturbations (Hoyle 1951; Peebles 1969; Doroshkevich 1970). This has been clarified and put together by White (1984) as the standard linear tidal-torque theory (TTT). According to TTT, the AM of the proto-haloes, dominated by dark matter (DM), grow linearly with time until they reach maximum expansion followed by collapse to virial equilibrium (quantified by simulations, e.g. Porciani, Dekel & Hoffman 2002a,b). The AM is predicted from the initial conditions by the asymmetric product of the tidal tensor T_{ij}, determined by the neighbouring fluctuation field, and the inertia tensor I_{ij}, characterizing the Lagrangian spatial distribution of the mass in the proto-halo.

The total AM of the halo is characterized by the dimensionless spin parameter (as defined by Bullock et al. 2001)

$$\lambda = \frac{j}{\sqrt{2}R_{\rm v}V_{\rm v}}\,, \qquad (1)$$

where $j = J/M$ is the magnitude of the specific angular momentum (sAM), namely the AM per unit mass within the halo, and $R_{\rm v}$ and $V_{\rm v}$ are the virial radius and velocity of the halo, respectively.[1] To

[1] In the Einstein-deSitter (EdS) phase, the virial radius and velocity are related to the virial mass $M_{\rm v}$ as $M_{\rm v12} \simeq (1+z)_3^{-3/2} V_{\rm v200}^3 \simeq (1+z)_3^3 R_{\rm v100}^3$, where $M_{\rm v12} = M_{\rm v}/10^{12}\,{\rm M}_\odot$, $V_{\rm v200} = V_{\rm v}/200\,{\rm km\,s^{-1}}$, $R_{\rm v100} = R_{\rm v}/100$ kpc, and $(1+z)_3 = (1+z)/3$.

★ E-mail: mark.danovich@mail.huji.ac.il

within the factor of $\sqrt{2}$,[2] λ measures the AM with respect to the maximum possible AM had all the mass been in a coherent circular orbit with a velocity $V_{\rm v}$ at $R_{\rm v}$. TTT predicts that the typical value of λ for DM haloes is universal, independent of halo mass and redshift (see below). Cosmological *N*-body simulations (Bullock et al. 2001) confirm this universality, and reveal that the distribution of λ among haloes is well fitted by a lognormal distribution, with a mean $\langle\lambda\rangle = 0.035 \pm 0.005$ and a standard deviation $\sigma = 0.50 \pm 0.03$ in natural log. A complementary way to view the AM history of DM haloes is through their buildup by mergers (e.g. Maller, Dekel & Somerville 2002).

In the standard picture, the baryons were expected to initially follow the DM mass distribution and share the same sAM distribution. This seemed natural in the case of a joint semi-spherical infall from outside the halo, and where the gas within the halo goes through a phase where it is pressure-supported after being heated to the virial temperature by a virial shock (Binney 1977; Rees & Ostriker 1977; Silk 1977). The hot gas is then assumed to cool radiatively, contract to the bottom of the spherical (or at least cylindrically symmetric) potential well while conserving AM, and form a central rotation-supported disc, whose density profile is dictated by the original distribution of AM within the halo (Fall & Efstathiou 1980; Fall 1983; Mo, Mao & White 1998; Bullock et al. 2001). This has been the basis for most analytic and semi-analytic modelling of galaxy formation. The predictions based on the simplified models are in the ball park of observed AM in low-redshift galaxies (e.g. Romanowsky & Fall 2012; Fall & Romanowsky 2013).

The developing new picture takes into account the fact that massive galaxies, in their most active phase of assembly and star formation at redshifts $z = 1$–4, form at the nodes of the cosmic web, where filaments intersect. This is a generic feature for massive galaxies at high redshift, as they emerge from high-sigma peaks of the density field. The evolution of the baryons in this framework has been tracked by high-resolution cosmological hydro-gravitational simulations, and understood by simple physics (Birnboim & Dekel 2003; Kereš et al. 2005; Cattaneo et al. 2006; Dekel & Birnboim 2006; Ocvirk, Pichon & Teyssier 2008; Dekel et al. 2009; Kereš et al. 2009). The baryons flow into the galaxies as streams that initially follow the central cords of the DM filaments. The streams of cold gas, at a few times 10^4 K, which at high redshift are narrow and dense compared to the halo, penetrate cold through the virial radius (Dekel et al. 2013), even if the halo is massive enough to support a shock in the rest of the virial shell ($M_{\rm v} \gtrsim 10^{12}\,{\rm M}_\odot$, Dekel & Birnboim 2006). In massive galaxies at high redshift, the streams also bring in the gas-rich merging galaxies, as a population of ex-situ clumps with a broad range of masses (e.g. Dekel et al. 2009).

In the inner halo, typically inside $\sim 0.3R_{\rm v}$, the simulations reveal that the streams enter a 'messy' interface region where they show a complex structure and kinematics (Ceverino, Dekel & Bournaud 2010, fig. 3) before they eventually join the central disc, typically inside a radius smaller than $0.1R_{\rm v}$. The nature and origin of this messy region is not yet understood, and it may involve break up and heating (Nelson et al. 2013), potentially by a combination of hydrodynamical, thermal and gravitational instabilities, shocks within the supersonic streams, and interactions of streams with other streams, with substructures, with the inner disc, and with outflows. The way the coherently inflowing supersonic streams eventually join the rotating disc is an open question of great interest, which we attempt to explore in this paper.

Being continuously fed by cold streams, the gas-rich disc tends to develop a violent disc instability (VDI), where the disc is turbulent and highly perturbed, with large transient features and *in situ* giant clumps (Noguchi 1999; Immeli et al. 2004; Genzel et al. 2006; Bournaud, Elmegreen & Elmegreen 2007; Genzel et al. 2008; Agertz, Teyssier & Moore 2009; Dekel, Sari & Ceverino 2009; Ceverino et al. 2010, 2012; Mandelker et al. 2014). Torques within the disc drive gas inflow and inward clump migration, which compactify the disc to drive central star formation in the form of a 'blue nugget' (Barro et al. 2013, 2014; Dekel & Burkert 2014; Zolotov et al. 2014), grow a massive rotating stellar bulge (Genzel et al. 2006, 2008; Bournaud et al. 2011; Ceverino et al. 2010, 2014b), and feed the central black hole (Bournaud et al. 2011).

The acquisition of AM by galaxies within this developing framework for galaxy formation is the challenge that we attempt to address here, following preliminary attempts (Pichon et al. 2011; Codis et al. 2012; Danovich et al. 2012; Stewart et al. 2013). The details of how galaxies are fed by elongated streams that originate in the cosmic web provide an explicit setting where TTT can be realized, possibly in a modified form. Then, the very non-spherical inflow through streams, their counter-rotating component, the interaction in the messy region at the greater disc environment, and the VDI processes in the disc, should all play major roles in the chain of events that lead to the AM buildup of galaxies, and they should be thoroughly investigated. In particular, one wonders to what extent the final AM in the disc is expected to differ from that implied by the simplified model based on spherical gas contraction conserving AM.

Danovich et al. (2012) used 1kpc-resolution cosmological hydro simulations with hundreds of massive galaxies to study the way they are fed at high-z by streams, focusing on the halo scales. The simulations reveal that the streams tend to be confined to a plane, the 'stream plane', which extends from inside the halo to a few virial radii. The stream plane is weakly (anti) correlated with the disc plane, consistent with TTT (see below). On average, 70 per cent of the influx through the virial radius is found to be in narrow streams, 67 per cent of it in one dominant stream, and 95 per cent in three major streams. It turns out that typically 87 per cent of the AM is carried by one dominant stream, the one with the highest product of mass inflow rate and impact parameter. This explains why the plane defined by the AM at $R_{\rm v}$ is only weakly correlated with the stream plane that involves the other streams. The virial AM plane itself is also found to be only weakly correlated with the inner disc plane, indicating a significant exchange of AM in the inner halo. This happens within the greater environment of the disc, the 'AM sphere' of radius $\sim 0.3R_{\rm v}$, which roughly coincides with the messy region seen in the simulations (Ceverino et al. 2010, fig. 3).

We propose here that the AM buildup in high-redshift galaxies consists of four phases that represent both stages of a time sequence and different spatial zones.[3] Phase I is the linear TTT phase, occurring in the cosmic web outside the halo, where the thin, elongated cold streams acquire more AM than the DM, expressed as impact parameters. Phase II is the transport phase, where the streams flow with a rather constant velocity and mass-inflow rate and roughly along straight lines down to $\sim 0.3R_{\rm v}$. Phase III is the strong-torque

[2] The factor $\sqrt{2}$ makes this spin parameter coincide with the earlier definition by Peebles (1969), $\lambda = J|E|^{1/2}G^{-1}M^{-5/2}$ (where E is the energy), in the case of a singular isothermal sphere truncated at $R_{\rm v}$.

[3] We note that while the phases and the zones are correlated, there is not always a one-to-one correspondence between them, and the boundaries between zones and between phases are not always sharp.

phase, in a tilted, inflowing, outer 'ring' at (0.1–0.3)$R_{\rm v}$. Finally, phase IV involves the inner disc and the growing bulge, where the final rearrangement of AM occurs due to VDI torques and feedback-driven outflows.

Here, we address this picture of AM buildup using a large suite of high-resolution zoom-in adaptive mesh refinement (AMR) hydro-cosmological simulations of massive galaxies at high redshift. The maximum resolution for the gas is ∼50 pc. We focus here on the average behaviour in the studied halo mass range ($10^{11.5}$–$10^{12.5}$ at $z = 2$) and redshift range ($z = 4 - 1.5$). We do not attempt to address the possible mass dependence and do not highlight the redshift dependence within these ranges – those are deferred to future work. Here, we are after the generic behaviour common to massive galaxies at high redshift, being fed by streams from the cosmic web.

The paper is organized as follows. In Section 2, we describe the cosmological simulations and the analysis of AM in them. In Section 3 to Section 6, we address each of the four phases, following the different components of baryons and DM with a special focus on the cold gas that dominates the supply to the growing disc. In Section 7, we provide a preliminary discussion of the robustness of our proposed scenario of AM buildup to variations in the assumed feedback based on simulations with stronger feedback. In Section 8, we summarize and discuss the proposed picture, its theoretical implications and its observational predictions.

2 METHOD

2.1 The cosmological simulations

Our cosmological simulations utilize the hydro-gravitational code ART (Kravtsov, Klypin & Khokhlov 1997; Kravtsov 2003), which uses AMR to follow the Eulerian gas dynamics. The code implements sub-grid models of the key physical processes relevant for galaxy formation. These include gas cooling by atomic hydrogen and helium, molecular hydrogen and metals, and photoionization heating by a UV background with partial self-shielding. Star formation is stochastic in cells with gas temperature $T \leq 10^4$ K and densities $n_H \geq 1\,{\rm cm}^{-3}$, at a rate consistent with the Kennicutt–Schmidt law (Kennicutt 1998). Stellar mass-loss and metal enrichment of the interstellar medium are included. Feedback from stellar winds and supernovae is implemented by injecting thermal energy to the neighbouring gas at a constant rate.

The cosmological model adopted in the simulation is the standard Λcold dark matter model with the *Wilkinson Microwave Anisotropy Probe 5* cosmological parameters ($\Omega_{\rm m} = 0.27$, $\Omega_\Lambda = 0.73$, $\Omega_{\rm b} = 0.045$, $h = 0.7$, $\sigma_8 = 0.82$) (Komatsu et al. 2009). Individual haloes were selected at $z = 1$ from an N-body DM-only simulation of a large cosmological box. Each halo and its environment were re-simulated at higher resolution with gas and the associated baryonic processes. The DM in each halo, out to a few virial radii, is typically represented by ∼10^7 particles of mass $6.6 \times 10^5\,{\rm M}_\odot$ each. The particles representing stars have a minimum mass of $10^4\,{\rm M}_\odot$. The AMR cells in the dense regions are refined to a minimum size in the range 35–70pc at all times. The adaptive refinement algorithm is such that a cell is divided into eight cells once it contains a mass in stars and DM more than $2 \times 10^6\,{\rm M}_\odot$, or a gas mass larger than $1.5 \times 10^6\,{\rm M}_\odot$. The force resolution is 1–2 grid cells of the maximum resolution. Artificial fragmentation on the cell size is prevented by introducing a pressure floor, which ensures that the Jeans scale is resolved by at least seven cells (see Ceverino et al. 2010). More details concerning the simulations are provided in Ceverino & Klypin (2009), Ceverino et al. (2010), Ceverino et al. (2012), Dekel et al. (2013) and Mandelker et al. (2014).

Table 1. The sample of simulated galaxies used in the main analysis of the current paper. Specified are the galaxy name, the halo virial mass, virial radius and disc radius at $a = 0.34$ ($z = 1$), and the expansion factor at the last snapshot used in the analysis, where $a = (1 + z)^{-1}$. More details are provided in Dekel et al. (2013, Table 1).

Galaxy	$M_{\rm v}$ ($10^{12}\,{\rm M}_\odot$)	$R_{\rm v}$ (kpc)	$R_{\rm d}$ (kpc)	$a_{\rm final}$
MW1	1.32	142	8.56	0.40
MW2	0.95	109	4.46	0.34
MW3	1.28	140	6.57	0.40
MW4	1.99	164	5.73	0.40
MW5	3.51	155	8.37	0.31
MW6	0.78	119	6.50	0.40
MW7	0.49	102	6.63	0.40
MW8	0.29	85	8.23	0.40
MW9	0.34	90	3.97	0.40
MW10	1.41	145	4.99	0.40
MW11	0.61	110	4.50	0.40
MW12	1.79	191	13.47	0.39
SFG1	1.98	154	10.73	0.38
SFG4	1.31	191	10.16	0.38
SFG5	1.74	155	6.33	0.40
SFG8	1.42	128	7.64	0.35
SFG9	3.54	198	9.39	0.40
VL01	1.89	149	3.53	0.37
VL02	0.93	126	9.99	0.40
VL03	1.16	114	6.71	0.32
VL04	1.20	137	4.23	0.40
VL05	2.08	165	12.23	0.40
VL06	0.82	121	6.46	0.40
VL07	1.63	130	6.00	0.34
VL08	1.13	135	5.91	0.40
VL09	0.54	91	3.21	0.34
VL10	1.09	133	3.34	0.40
VL11	1.98	163	3.29	0.40
VL12	1.04	131	5.60	0.40

Our sample consists of 29 galaxies in the redshift range $z = 4 - 1.5$, listed in Table 1. The virial masses at $z = 2$ are in the range $10^{11.5}$–$10^{12.5}\,{\rm M}_\odot$. The haloes were selected not to undergo a major at or near $z \sim 1$. This turned out to eliminate about 10 per cent of the haloes in the selected mass range. More details concerning the sample are listed in table 1 of Dekel et al. (2013) and discussed there.

Several limitations of the simulations used here, mostly in terms of how star formation and feedback are implemented, are described in Section 7. In order to evaluate the possible sensitivity of our results to feedback strength, we briefly refer there to preliminary results from an improved suite of simulations, with higher resolution, lower star formation rate (SFR) efficiency, and stronger feedback. These simulations fit observations better, and will be analysed in detail in a future paper. We find that the results reported here are qualitatively robust, with non-negligible effects limited to the AM distribution within the inner disc. In the visual study of gas in the inner halo, Section 5, we make a very limited use of two snapshots from the new simulations, which are listed at the bottom of Table 2.

Table 2. Snapshots of galaxies used in the analysis in specific sections and figures. Each snapshot is identified by the galaxy name and the redshift, and the quantities quoted are the virial mass $M_{\rm v}$ and radius $R_{\rm v}$, as well as the stellar and gas mass within the galaxy, M_* and $M_{\rm g}$, and the disc radius $R_{\rm d}$. The two snapshots identified as VEL are from a new suite of simulations with higher resolution, lower SFR efficiency and stronger feedback, that are used only in one illustrative picture and not in the quantitative analysis.

Galaxy	$M_{\rm v}$ ($10^{12}\,{\rm M}_\odot$)	M_* ($10^{11}\,{\rm M}_\odot$)	$M_{\rm g}$ ($10^{11}\,{\rm M}_\odot$)	$R_{\rm v}$ (kpc)	$R_{\rm d}$ (kpc)	z
MW1	1.16	1.14	0.65	129	4.5	1.63
MW3	0.36	0.26	0.31	70	5.3	2.33
MW8	0.23	0.22	0.12	61	4.3	2.33
SFG1	1.27	1.41	0.60	86	10.0	3.17
SFG8	1.06	1.23	0.50	86	3.6	2.92
SFG8	1.22	1.38	0.60	98	5.9	2.57
SFG8	1.35	1.56	0.77	114	6.8	2.17
VL01	0.97	1.10	0.49	91	5.1	2.57
VL01	1.01	1.16	0.52	95	6.5	2.45
VL02	1.08	1.27	0.59	141	9.7	1.33
VL11	1.98	2.43	1.17	163	8.8	1.50
VEL3	0.19	0.07	0.13	74	9.4	1.50
VEL7	1.49	1.23	0.77	169	18.1	1.17

2.2 Angular momentum of different components

The instantaneous position of the origin of the frame of reference and the velocity rest frame for each galaxy were determined by the centre of mass of the inner stellar particles. The relevant inner sphere was chosen to contain at least 20 stellar particles within a radius of 130 pc or larger, and it has been positioned through an iterative procedure that maximizes the stellar density within it. The positions and velocities of the gas, stars and DM particles were all corrected to this origin and rest frame, and the AM is always measured in this frame with respect to the galaxy centre. In order to test robustness, the analysis has been repeated with alternative definitions of rest frame, such as the centre-of-mass velocity of the gas within $R_{\rm v}$, yielding differences of the order of 10 per cent in spin parameter. When referring to AM changes due to torques, we ignore the fact that the sequence of instantaneous rest frames do not define a proper inertial frame.

Throughout the paper, we consider the AM of different mass components, distinguishing DM from baryons, and considering cold gas, hot gas and stars. The gas is defined as 'hot' if its temperature is higher than 10^5 K and higher than the temperature of the shock-heated gas, $T_{\rm s} = 3T_{\rm v}/8$, where $T_{\rm v}$ is the virial temperature, $T_{\rm v} = 1.44 \times 10^5\,{\rm K}\,V_{\rm v200}^2$ (Dekel & Birnboim 2006). For the masses and redshifts analysed, this threshold temperature is typically a few times 10^5 K. The gas is defined as 'cold' once the gas temperature is below 10^5 K, and the gas density is above a number density threshold of $100\,\bar{n}_H$, where $\bar{n}_H \simeq 2 \times 10^{-7}\,{\rm H\,cm^{-3}}(1+z)^3$ is the mean cosmological number density of hydrogen. This density threshold was chosen such that the cold streams are clearly revealed at large distances by visual inspection (also adopted by Kimm et al. 2011). This threshold eliminates only 4 per cent of the cold gas within the virial radius, and 44 per cent outside it, so it is effective mostly outside the virial radius. The gas fraction with a temperature in the range between 10^5 K and $T_{\rm s}$ (when $T_{\rm s} > 10^5$ K), namely the gas that falls between the cold and hot components as defined here, is on average 9 per cent within (0.1–1) $R_{\rm v}$ and 22 per cent at (1–2) $R_{\rm v}$. We find that the results not sensitive to moderate variations in the above temperature and density criteria. In limited cases specified below, dense cold gas in clumps is eliminated above $10^3\bar{n}_H$ in order to reduce wild fluctuations. There is a practical upper limit for the gas density above $\sim$1 cm^{-3}, the built-in density threshold for star formation in the simulations, though this is not a strict limit because the star formation is stochastic.

3 PHASE I: TIDAL TORQUES IN THE COSMIC WEB

3.1 Summary of tidal-torques theory

The first stage in the origin of the AM in galaxies takes place when the streams are part of the cosmic web before they enter the halo, typically at a distance of two to a few virial radii from the halo centre. The TTT for the origin of halo AM has been developed by White (1984) based on the pioneering work of Peebles (1969) using the Zel'dovich approximation in the quasi-linear regime, and has been tested using cosmological N-body simulations (Porciani et al. 2002a,b). The basic ideas of TTT are robust and could be still valid, possibly with some modifications, so it is worth summarizing here before we proceed to the analysis of the simulations.

According to TTT, the final AM of the halo is determined in the proto-halo stage in the linear regime, by the gravitational coupling of the tidal field generated by neighbouring fluctuations and the quadrupole moment of the Lagrangian volume of the proto-halo, Γ. The spatial dependence of the components of the AM vector $\boldsymbol{J}$ are given by the antisymmetric tensor product

$$J_i \propto \epsilon_{ijk}\boldsymbol{T}_{jl}\boldsymbol{I}_{lk}\,. \tag{2}$$

The tensor $\boldsymbol{T}_{jl}$ is the tidal tensor,[4]

$$\boldsymbol{T}_{jl} = -\frac{\partial^2\phi}{\partial q_j \partial q_l}\,, \tag{3}$$

where ϕ is the gravitational potential and $\boldsymbol{q}$ refers to the Lagrangian, comoving coordinates. The tidal tensor is evaluated at the centre-of-mass of Γ, using a second-order Taylor expansion of the potential. The tensor $\boldsymbol{I}_{lk}$ is the inertia tensor of Γ,

$$\boldsymbol{I}_{lk} = \bar{\rho}\,a\int_\Gamma q_l q_k {\rm d}^3 q\,, \tag{4}$$

where $\bar{\rho}$ is the mean density at the time when the universal expansion factor is a. The traceless part of $\boldsymbol{I}_{lk}$ is the quadrupolar inertia tensor. It follows from equation (2) that the traceless parts of these tensors can be used without changing the resultant AM. We learn from equation (2) that a net AM is generated due to the deviation of the proto-halo from spherical symmetry and the misalignment of the eigenvectors of these two tensors, which is found in simulations to be non-zero but rather small. This is why the halo is far from being supported by rotation, with a spin parameter of only a few per cent.

In the principle coordinates of the inertia tensor, the AM components are given by

$$J_1 \propto T_{23}(I_3 - I_2),\ J_2 \propto T_{13}(I_1 - I_3),\ J_3 \propto T_{12}(I_2 - I_1), \tag{5}$$

where I_i are the corresponding eigenvalues ordered from large to small. This implies that J_2, the AM component along the intermediate axis of the inertia tensor of Γ, for which $|I_1 - I_3|$ refers to the difference between the major and minor eigenvalues, has the highest probability to be the largest AM component (see applications

[4] The tensor as expressed here is commonly termed the 'deformation' tensor, and its traceless part is referred to as the 'tidal', or 'shear' tensor.

to disc alignment with large-scale structure in Navarro, Abadi & Steinmetz 2004; Hahn, Teyssier & Carollo 2010).

In the linear regime, as the perturbation associated with the proto-halo grows, TTT predicts that the AM of the proto-halo grows in proportion to $a^2D(a)$, where $D(a)$ is the growing mode of linear perturbations. In the Einstein-deSitter (EdS) regime, this growth is linear with time,

$$J_i \propto a^2 D(a) \propto t\,. \tag{6}$$

It has been confirmed in N-body simulations (Porciani et al. 2002a,b) that the acquisition of AM significantly slows down once the proto-halo reaches maximum expansion, at twice its current virial radius according to the spherical collapse model, after which it turns around and collapses to the virialized halo within the virial radius. After maximum expansion, the tidal torques become inefficient due to the declining moments of inertia, so the AM remains roughly fixed during the collapse and virialization.

From the above basics of TTT one can derive the universality of the halo spin parameter in terms of halo mass $M_{\rm v}$ and expansion factor at virialization $a_{\rm v}$, as follows. The tidal tensor in equation (2) scales as $\nabla^2\phi$ in Lagrangian space. The time of maximum expansion, corresponding to an expansion factor $a_{\rm max}$, can be identified as the time when the linearly growing density fluctuation of the proto-halo, δ, reaches a value of the order of unity. Based on linear theory of fluctuation growth, one can write $\delta \propto D(a)\nabla^2\phi$. Therefore, when $\delta \sim 1$, one has $\nabla^2\phi \propto D(a_{\rm max})^{-1}$. In the EdS regime, this is $D^{-1} \propto a_{\rm max}^{-1} \propto a_{\rm v}^{-1}$. The inertia tensor in equation (2), per unit mass, scales like R^2, where R is the comoving size of Γ, namely $R^2 \propto M_{\rm v}^{2/3}$. Put together using equations (2) and (6), one obtains for the sAM in the halo $j \propto a_{\rm v}^{1/2} M_{\rm v}^{2/3}$. Indeed, one can deduce from the standard virial relations that the same scaling applies for the combination $R_{\rm v}V_{\rm v}$ by which j should be divided in order to evaluate λ in equation (1). The DM halo spin λ is therefore predicted to be independent of both $M_{\rm v}$ and cosmological time. This has been confirmed using cosmological N-body simulations (Bullock et al. 2001; Bett et al. 2007).

3.2 Dark matter spin profile

Fig. 1 shows the spin-parameter radial profile (namely the sAM profile $j(r)$ normalized by $\sqrt{2}R_{\rm v}V_{\rm v}$, equation 1) averaged over all the simulated haloes. The sAM is computed in shells of thickness $0.1R_{\rm v}$ at radii in the range $r = (0.1\text{–}2)R_{\rm v}$. The profiles are shown for the different mass components at three different redshifts.

The DM spin profiles show a universal linear shape at all times, roughly

$$j(r) \propto r\,, \tag{7}$$

rising from $\lambda(r) \sim 0.011$ at $0.1R_{\rm v}$ to 0.22 at $2R_{\rm v}$. The self-similarity in time of the DM spin distribution follows from TTT, as argued above. The linear shape of the profile for the DM is consistent with earlier findings within virialized haloes using N-body simulations (Bullock et al. 2001; Bett et al. 2010), and with analytic predictions derived using a simple toy model that incorporates the combined effects of tidal stripping and dynamical friction on the merging sub-haloes that build the host halo as they spiral in, assuming a halo with a density profile close to that of an isothermal sphere (Bullock et al. 2001).

An interesting feature in Fig. 1 is that the same profile seems to extend from inside the halo out to $2R_{\rm v}$ and possibly beyond. This may partly reflect the fact that the region where the DM has been mixed actually extends beyond the formal virial radius defined by a given overdensity of ∼200 (Prada et al. 2006), so the tidal stripping and dynamical friction are active already at larger radii, thus explaining the extension of the $j \propto r$ profile to beyond $R_{\rm v}$.

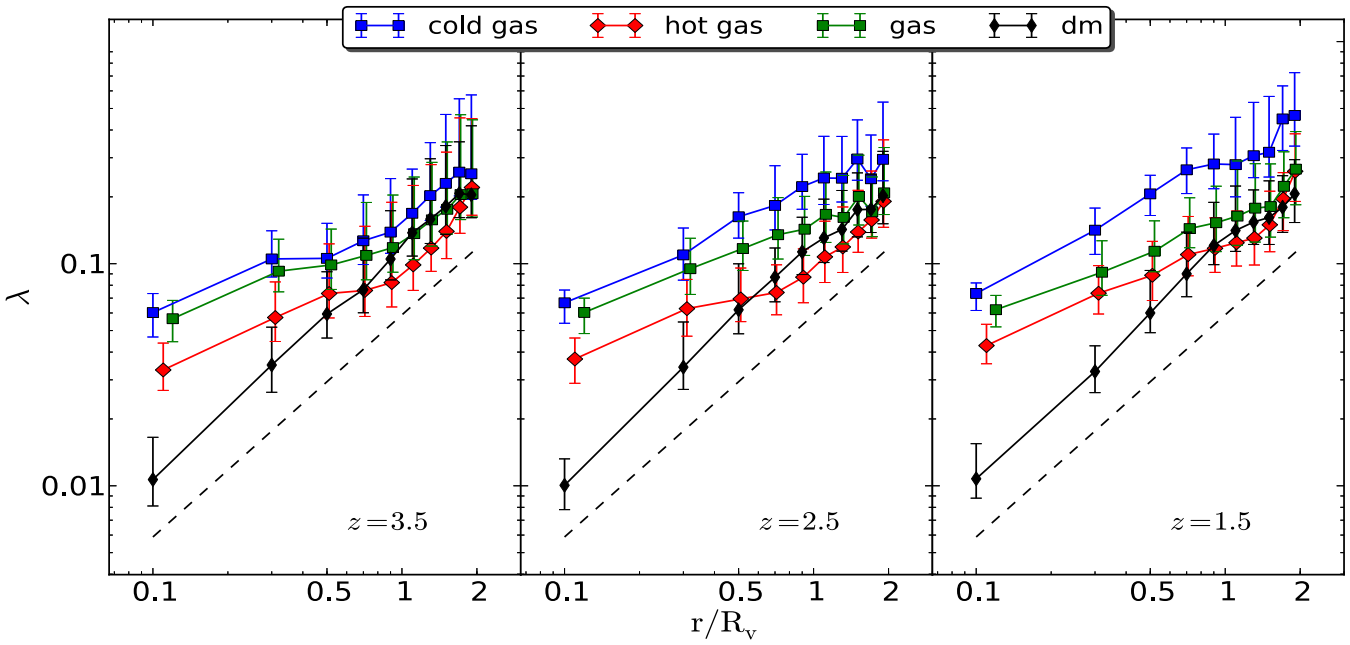

Figure 1. Radial profiles of the spin parameter, $\lambda(r/R_{\rm v}) = j(r/R_{\rm v})/(\sqrt{2}R_{\rm v}V_{\rm v})$, where j is the specific AM in a shell of radius $r/R_{\rm v}$, averaged over all haloes from Table 1 at three different redshifts. The curves refer to the different mass components of cold dense gas, hot gas, all the gas and dark matter. The sAM is computed in shells of thickness $0.1R_{\rm v}$. Shown are the mean and standard deviation. The dashed line are of slope unity. In zone I and II, the dark matter spin profile is roughly linear with radius and self-similar in time. The spin of cold gas is higher, by a factor of 1.3–2 outside the halo and by a factor of a few inside the halo.

It is worth noting that a monotonically increasing $j(r)$ profile is expected already in the inflowing region outside $R_{\rm v}$ based on TTT. This is because a shell that is now at an earlier stage of its infall towards $R_{\rm v}$ started from a larger Lagrangian radius and thus had a larger quadrupole moment, and because it reached maximum expansion at a later time. According to the spherical-collapse model, with the virial radius at half the maximum expansion radius of the shell now crossing $R_{\rm v}$, a simple calculation shows that $j(2R_{\rm v})/j(R_{\rm v}) \simeq 1.4$, corresponding to an effective power-law fit of roughly $j(r) \propto r^{0.5}$ in the range (1–2)$R_{\rm v}$. This is an increase with r, but slightly shallower than what is seen in Fig. 1. However, there is indeed a hint for a shallowing of the profile outside $R_{\rm v}$ at the later redshifts. The deviation may hint for a partial failure of the spherical model to account for the strong deviations from spherical symmetry associated with the inflowing DM streams. Alternatively, as suggested above, it may reflect the effects of tidal stripping and dynamical friction already outside the formal virial radius.

We should point out that the rising $\lambda(r)$ outside the halo is not in conflict with the expected universal value for λ within DM haloes. This is because when a shell that is now at $r > R_{\rm v}$ will enter the virial radius with its larger j, the normalization factor $R_{\rm v}V_{\rm v}$ will also be larger due to the halo growth during that period, such that the obtained λ within the halo will be the same as it is now.

We see in Fig. 1 that the spin parameter of the DM shell upon entry of the virial radius is $\lambda \simeq 0.13$ at all times. We will see that the average over the whole halo is $\lambda \simeq 0.04$, similar to the findings in previous studies (Bullock et al. 2001; Bett et al. 2007).

3.3 Cold gas outside the halo

The most interesting finding from Fig. 1 is that outside the virial radius the spin parameter of the cold gas is higher than that of the DM, by a factor of 1.5–2, a factor that grows with cosmic time. A similar phenomenon has been detected in other simulations (Kimm et al. 2011; Pichon et al. 2011; Powell, Slyz & Devriendt 2011, Tillson et al. 2012, Stewart et al. 2013). The spin parameter of the cold gas upon entry through the virial radius varies from $\lambda \simeq 0.2$ at $z = 3.5$ to $\lambda \simeq 0.3$ at $z = 1.5$, compared to the 0.13 of the DM. This trend continues beyond $2R_{\rm v}$ (beyond the radii shown in the figure). The origin of this, to be addressed next, could in principle be due to gravitational torques, involving different quadrupole moments for the two components while the tidal tensor acting on both is similar and so is its misalignment with the inertia tensors of the two components. Alternatively, the difference between the spins of cold gas and DM could possibly be due to pressure torques that act on the gas only (see Section 3.4 below).

Fig. 2 shows maps of projected gas density and the corresponding z-component sAM in the face-on disc frame for the different mass components in snapshots of two simulated galaxies. One can clearly see that the mass and AM are carried from well outside the halo into its central region by elongated, rather straight streams. While the cold-gas streams are rather narrow, the DM streams are much thicker, with a non-negligible component of inflow from a wide angle between the large streams. The gas has dissipatively contracted into the cords of the DM filaments at an earlier stage, but outside the halo the gas distribution is still elongated and possibly still in its expansion phase along the filament in the radial direction away from the galaxy. While in the spherical collapse model, there is a single maximum-expansion event for each shell, here the relevant maximum expansion is along the filament, when the torques are most effective. Therefore, it is the quasi-linear Eulerian inertia tensor near this moment that is relevant. Fig. 2 indicates that the quadrupole moment of the cold gas outside the halo is significantly larger than that of the DM.

Fig. 3 shows a crude estimate of the ratio of the quadrupole moments for cold gas and DM outside the halo. The instantaneous inertia tensor of each mass component is computed and diagonalized within the shell (1–2)$R_{\rm v}$ in each galaxy. The eigenvectors of the two components are found to be well aligned in most cases. Under the assumption that the tidal tensor that exerts torques on the two components is practically the same, we conclude that the non-vanishing mutual misalignment of the tidal and inertia tensors (studied for the DM in Porciani et al. 2002a,b) is similar for the two components, so the difference in AM should arise from the magnitude of the eigenvalues. We use the eigenvalue differences $I_j - I_k$ as proxies for the quadrupole moments. Shown in the figure are the average ratios of these differences for the cold gas and the DM. We learn that the quadrupole moment of the cold gas is consistently higher than that of the DM by a factor of 1.5–2, which is increasing with cosmic time. This implies that the sAM of the cold gas outside the halo should be higher by a similar factor, as indeed seen in Fig. 1. This indicates that TTT is crudely valid once applied to the large-scale mass distribution in the elongated thin streams outside the halo where they are near their maximum expansion. The validity of TTT is allowed in this quasi-linear regime by the fact that the Zel'dovich approximation used in the TTT analysis is a good approximation in this regime near pancake and filament configurations. We can conclude that the higher spin parameter of the cold gas at the virial radius predominantly originates from its larger quadrupole moment in the TTT phase outside the halo. This confirms and explains the conjecture made by Stewart et al. (2013).

As a result of the tidal torques acting prior to maximum expansion, each of the cold streams, which originally tend to be pointing to the halo centre, obtains a non-zero impact parameter. This can be interpreted as generated by asymmetric flows from voids and sheets into the streams from the transverse directions to the streams (Pichon et al. 2011; Codis et al. 2012). The largest impact parameter is typically $b \sim 0.3R_{\rm v}$. Since the stream velocity is typically $\sim 1.5V_{\rm v}$, this corresponds to $\lambda \sim 0.3$ at pericentre for the streams that carries the largest AM. The other streams acquire smaller impact parameters, and sometime contribute AM in the opposite direction, as can be seen in the two galaxies shown in Fig. 2 for the streams that come from the left. The mixing of AM from streams with large and small (or even opposite-sign) impact parameters tends to lower the net spin brought into the inner halo by the cold gas to $\lambda \sim 0.1$.

One can see in Fig. 2 that beyond the virial radius the spin parameter of the hot gas is closer to the spin of the DM than that of the cold gas. This is consistent with the wide-angle distribution of the hot gas that is closer to that of the DM and thus has a similar quadrupole moment.

Our analysis indicates that TTT, once modified to account for the pre-collapse of the gas to the cords of the filaments, provides a sensible qualitative description of the initial acquisition of AM by the cold gas outside the halo from the cosmological environment. For a more quantitative analysis, one may suspect that some of the additional assumptions made in standard TTT, such as the second-order expansion of the potential about the halo centre, may not be accurate enough given the deviations from spherical symmetry associated with elongated streams that stretch to a few virial radii, and should be modified.

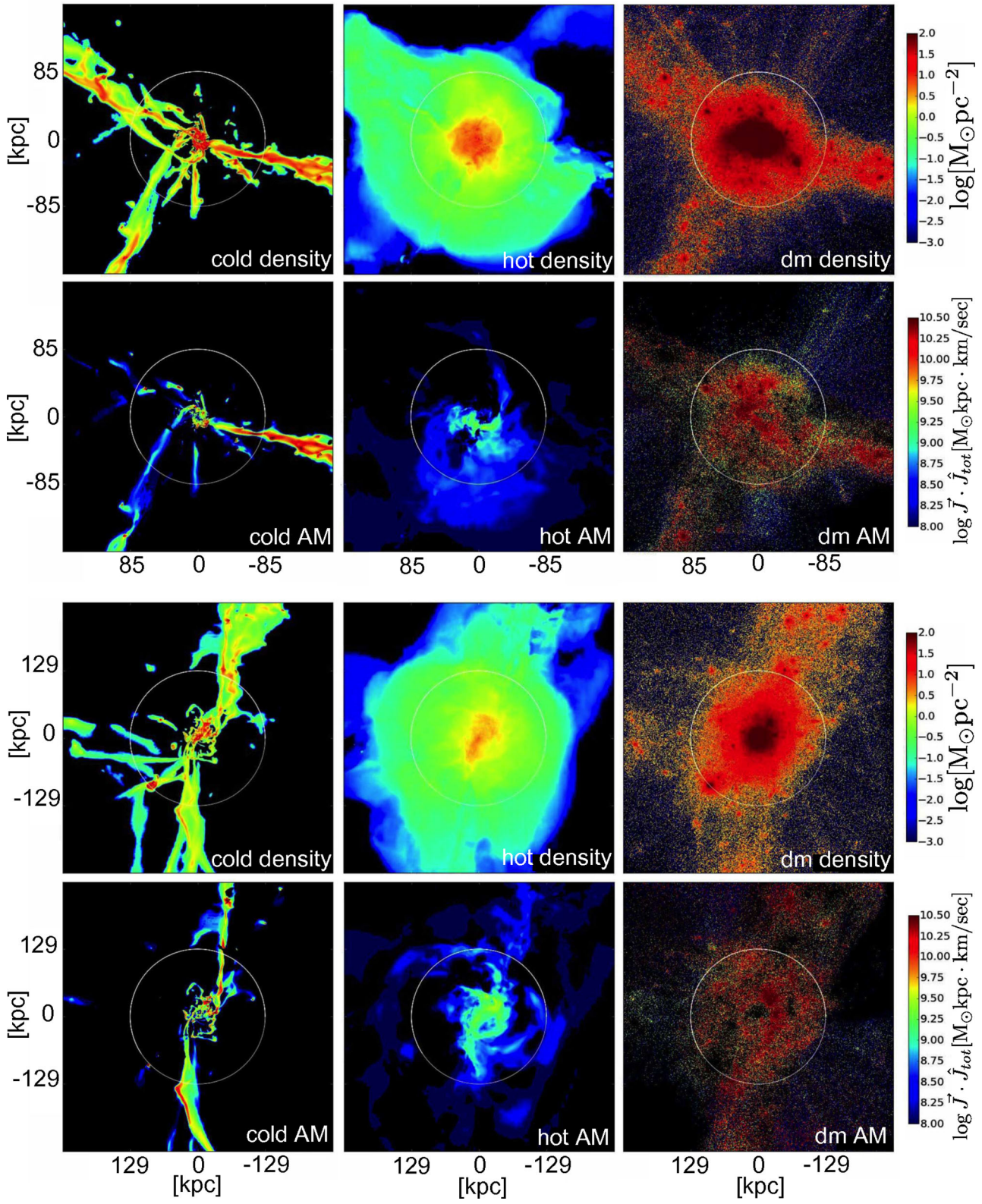

Figure 2. Surface density (top) and positive AM (bottom) for the different mass components in two galaxies from Table 2 (top two rows SFG1 $z = 3.17$, bottom two rows MW1 $z = 1.63$). The components are cold gas (left), hot gas (middle) and dark matter (right). The view is face-on in the disc plane. The cubic box is of side $2R_{\rm v}$, with $R_{\rm v}$ marked by the circle. The positive AM component shown is in the direction of the total AM vector of the given mass component within the halo. In zone I (and II), the cold streams are much thinner and more coherent than the dark matter inflows.

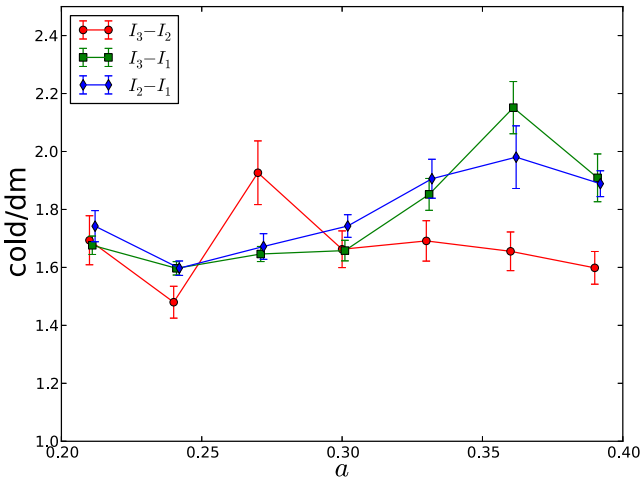

Figure 3. The ratio of quadrupole moments for cold gas and dark matter in the shell (1–2)$R_{\rm v}$ averaged over all snapshots. Shown as a function of expansion factor a are the medians of the ratios of the quantities $I_j - I_k$, the differences between the eigenvalues of the inertia tensors that appear in equation (5). The error bars refer to the errors of the mean. The quadrupole moments of the cold gas in zone I (and II) are larger than those of the dark matter by a factor of 1.5–2, reflecting the thin nature of the cold streams compared to the thick filaments and the wide-angle distribution of inflowing dark matter.

3.4 Gravitational versus pressure torques

The AM per unit volume of a fluid in a given position $\boldsymbol{r}$, where the density is ρ and the velocity is $\boldsymbol{r}$, is

$$\boldsymbol{l} = \rho\, \boldsymbol{r} \times \boldsymbol{v}\,. \tag{8}$$

Its Eulerian rate of change, $\partial \boldsymbol{l}/\partial t$, can be expressed in terms of the gravitational force and the pressure gradient (plus other terms) using the continuity equation and Euler's equation of motion. After some algebra, and subtracting off the advection term, one obtains the Lagrangian torque, $d\boldsymbol{l}/dt$, as a sum of three terms:

$$\boldsymbol{\tau} = \boldsymbol{\tau}_\phi + \boldsymbol{\tau}_{\rm p} + \boldsymbol{\tau}_s = -\rho\, \boldsymbol{r} \times \nabla\phi - \boldsymbol{r} \times \nabla P - \boldsymbol{l}\, \nabla \cdot \boldsymbol{v}\,, \tag{9}$$

where ϕ and P are the gravitational potential and the pressure at $\boldsymbol{r}$, respectively.

The first term $\boldsymbol{\tau}_\phi$ is the torque due to the gravitational force acting on all the mass components. Since the torque is measured with respect to the disc centre, a non-zero torque requires a non-radial force component. Possible sources for such a torque on large scales are the non-uniform mass distribution in the cosmic web including neighbouring haloes and subhaloes. Within the inner halo, gravitational torques could result for example from dynamical friction acting on the clumpy components by the smooth DM distribution, or from the gravitational field generated by the disc.

The second term $\boldsymbol{\tau}_{\rm p}$ is the torque resulting from a pressure gradient, acting only on the gas. The pressure torque may be important in the interface between hot and cold gas where a pressure gradient may be present. We note that it may depend on the resolution, but one may expect a smaller contribution of the pressure torques once the boundary layer between cold and hot gas is better resolved, where this layer may become unstable.

The third term is the strain associated with the viscosity that couples the off-diagonal elements in the stress tensor to the hydro equations. Being a vector proportional to the AM vector itself, the strain can only change the magnitude of the AM. Since the viscosity in the simulations is only a small numerical viscosity, this term turns out to be negligible compared to the other two.

We define dimensionless parameters that measure the potential ability of the pressure and gravitational torques to make substantial changes in the AM of a given fluid element during the characteristic time-scale $t_{\rm torq}$ over which the torques are acting,

$$q_\phi = t_{\rm torq}\frac{|\vec{\tau}_\phi|}{|\vec{l}\,|}, \quad q_p = t_{\rm torq}\frac{|\vec{\tau}_{\rm p}|}{|\vec{l}\,|}\,. \tag{10}$$

At a distance $\sim f R_{\rm v}$ from the galaxy centre, the relevant time-scale could be the corresponding fraction of the virial time-scale ($t_{\rm v} = R_{\rm v}/V_{\rm v}$), namely $t_{\rm torq} \sim f t_{\rm v}$. For example, for an $M_{\rm v} \sim 10^{12}\,{\rm M}_\odot$ halo at $z \sim 2$, $t_{\rm v} \sim 0.5$ Gyr. This means that outside the halo, at $f \sim 2$ say, we would consider $t_{\rm torq} \sim 1$ Gyr. In the inner halo, say at $f \sim 0.2$, we would typically use $t_{\rm torq} \sim 100$ Myr for radial inflow, but several hundred Myr for gas spiralling in along a quasi-circular orbit.

The gravitational torque is calculated from the gravitational potential at each point, computed with a softening length of four grid cells via a tree-code algorithm (Barnes & Hut 1986). The mass distribution in each of the cubic tree nodes is represented by a multipole expansion to quadrupole order. The accuracy of the force calculation is then controlled by the ratio θ of the size of the node exerting the force and the distance from the centre of mass of this node to the particle or cell on which the force is exerted, which has been set to $\theta = 0.8$ for a better than 1 per cent accuracy. The spatial derivatives of the potential are calculated on a uniform grid extracted from the AMR grid using a tri-cubic spline interpolation scheme.

Fig. 4 shows maps of the ratio of gravitational and pressure torques acting on the cold gas, $\log|\tau_\phi|/|\tau_p|$, in two galaxies. The maps are projections face-on in the stream plane as defined at $R_{\rm v}$, meant to optimize the view of the cold streams. The visual impression is that the gravity torques dominate along the streams as well as in the central disc vicinity. In the regions where the contribution of the pressure torques are comparable to the gravitational torques (white), the torque itself tends to be small compared to where the gravity torques dominate. The regions where the pressure torques dominate (red), typically in the boundaries of the cold streams, tend to contain a small fraction of the cold gas, and the torques acting from all sides of the filaments tend to cancel each other such that they do not produce substantial net AM.

Indeed, Fig. 5 compares radial profiles of q_ϕ and $q_{\rm p}$ for the cold gas. The torques $\boldsymbol{\tau}$ and the AM $\boldsymbol{l}$ in equation (10) were integrated in shells of thickness $0.1R_{\rm v}$, and $t_{\rm torq}$ was set to $0.5t_{\rm v}$. These torques were computed for the cold gas, with the dense clumps eliminated by excluding gas densities higher than 1000 times the mean hydrogen density. For the snapshots used, at $z \sim 2-3$, this upper limit for the density is $\sim 10^{-2}\,{\rm cm}^{-3}$. This removes fluctuations and generally lowers the q values, but it does not affect the ratio of q_ϕ and $q_{\rm p}$. The profiles shown were generated by stacking six snapshots from Table 2. One can see that the net contribution of the pressure torques is negligible – it could make only small changes to the AM and it is much smaller than the gravitational torques at all radii.

The fact that the averaged q_ϕ is larger than unity implies that the gravitational torques are capable of having a significant effect on the AM near and outside $R_{\rm v}$. The fact that q_ϕ is roughly constant in radius implies that the torques could be more effective at larger radii, namely outside the halo, because the time spent there is longer. This is both because of the longer distance and the slower velocity at larger radii in the free-fall regime outside $R_{\rm v}$.

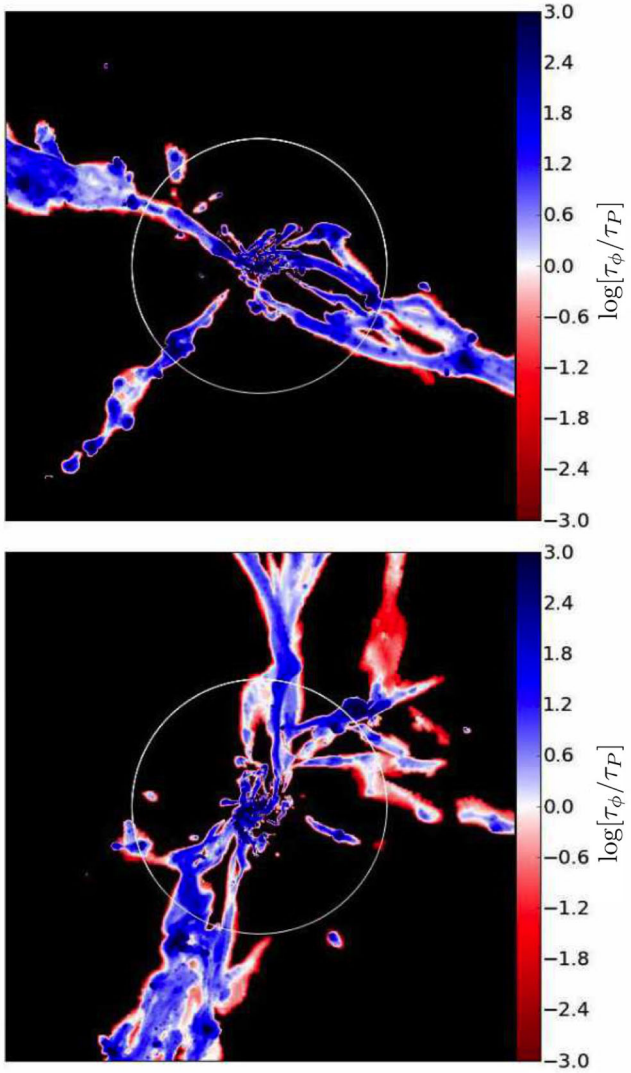

Figure 4. The ratio of gravitational to pressure torques acting on the cold gas, $\log|\tau_\phi|/|\tau_\mathrm{p}|$. Shown are projections in the direction of the stream plane as defined at R_v for SFG1 $z = 3.17$ (top) and MW1 $z = 1.63$ (bottom). The circle marks the virial radius. The gravitational torques dominate almost everywhere.

In summary for phase I, the AM is acquired by gravitational torques outside R_v. The sAM gained by the cold gas is larger than the sAM gained by the DM by a factor of 1.5–2 due to the higher quadrupole moment resulting from the early dissipative contraction of gas into the central cords of the rather thick DM filaments. It is encouraging that a similar result is obtained from different simulations using different codes (e.g. Kimm et al. 2011; Stewart et al. 2013).

4 PHASE II: AM TRANSPORT THROUGH THE HALO

4.1 Dark matter in the halo

The second phase takes place as the inflowing streams approach the virial radius and penetrate through the outer halo, typically between $2R_\mathrm{v}$ and $0.3R_\mathrm{v}$. In this regime, the DM particles virialize. The ones that flow in later with higher sAM tend to settle in more

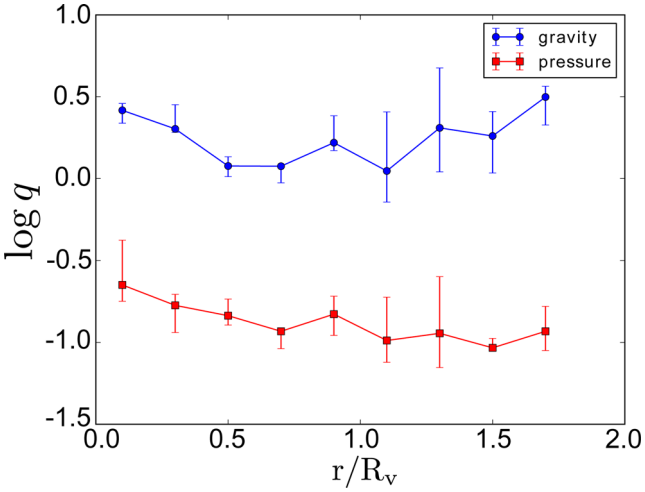

Figure 5. Profiles of gravitational and pressure torques, q_ϕ and q_p (equation 10), acting on the cold gas, with dense clumps eliminated. The vectors of torque τ and AM l are integrated in shells of thickness $0.1R_\mathrm{v}$, and $t_\mathrm{torq} = 0.5t_\mathrm{v}$. These profiles are generated by stacking six snapshots from Table 2 (MW1 $z = 1.63$, MW3 $z = 2.33$, MW8 $z = 2.33$, SFG1 $z = 3.17$, SFG8 $z = 2.17$, VL01 $z = 2.57$). The net contribution of the pressure torques is negligible compared to the gravitational torques at all radii.

extended orbits, but they partly mix with the DM that is already there with lower sAM. The total spin parameter within R_v is therefore significantly lower than that of the recently arrived particles. Fig. 6, top-left panel, shows the probability distribution of the spin parameter for the DM within R_v over all haloes and snapshots. The distribution is well fitted by a lognormal distribution with a mean $\langle\lambda\rangle = 0.038$ and standard deviation $\sigma = 0.59$, in fair agreement with the findings from pure N-body simulations of more massive haloes (Bullock et al. 2001). Fig. 7 demonstrates that the average λ for the DM within the halo is the same at all times, as predicted by TTT and as seen in the earlier simulations. Recall that Fig. 1 showed that the radial profile is roughly $j(r) \propto r$, consistent with the simulation results and with a toy model for halo buildup by tidal stripping of satellites as they spiral in by dynamical friction (Bullock et al. 2001).

4.2 Cold gas in penetrating streams

Contrary to the DM, the streams of cold gas penetrate through the outer halo at a velocity that is comparable to and slightly higher than V_v without significant mixing with the lower sAM gas that flew in earlier and is now either in the central disc and its vicinity or it has been heated and removed by feedback. Fig. 6 shows that the distribution of λ for the cold gas in the halo, excluding the inner $0.1R_\mathrm{v}$, is well fit by a lognormal distribution with a mean $\langle\lambda\rangle = 0.11$. This is a factor of $\sim$2.5 larger than that of the DM in the same volume, partly due to the higher sAM gained by the cold gas in zone I outside the halo, and partly due to the mixing of the incoming DM with lower sAM DM within the halo. A similar difference between the spin of the cold gas in the halo and that of the DM has been detected in other simulations (Sharma & Steinmetz 2005; Kimm et al. 2011; Stewart et al. 2011). The previously accreted, lower sAM cold gas, if not removed by outflows, is largely confined to the galaxy at $r < 0.1R_\mathrm{v}$, as cold gas and stars, with a lower spin parameter. This spin parameter of the galactic baryons is strongly affected by the very low spin of the massive stellar bulge, reflecting the AM loss by the cold gas in the inner halo and the disc (Sections 5

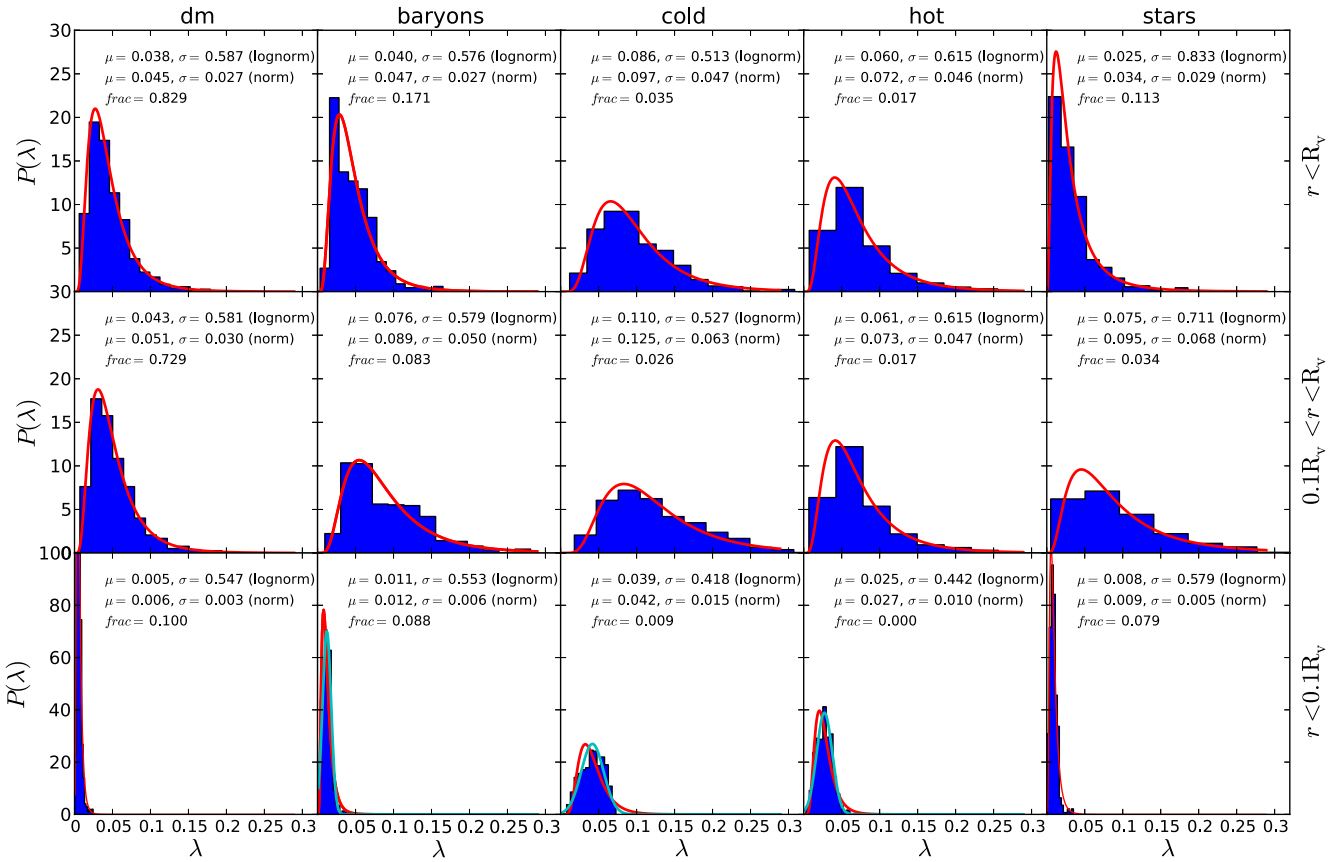

Figure 6. Spin parameter probability distribution for different components within the halo at three radial ranges, over all galaxies and snapshots. The 'baryon' component is the sum of the 'cold', 'hot' and 'stars' components. The spin λ refers to the sAM j, while the direction $\hat{J}$ may be different for each component and for each zone. Shown are lognormal fits (red) and Gaussian fits (light blue, shown only for $r < 0.1R_v$), and the corresponding mean μ and standard deviation σ i are quoted. Also quoted is the mass fraction *frac* of each component relative to the total mass in the halo. The spin of cold gas in the halo is higher than that of the dark matter by a factor of ∼3. It is larger by an order of magnitude than the spin of the baryons at $r < 0.1R_v$.

and 6). Evidence for this AM loss is in the fact that inside R_v the average spin parameter of the baryons, $\langle\lambda_{bar}\rangle = 0.040$, is comparable to that of the DM, despite the fact that most of the baryons entered the halo cold with a spin parameter that was higher by a factor of 1.5–2.

Fig. 7 reveals that the average λ for the halo cold gas gradually grows with time roughly linearly with expansion factor a, from about 0.08 at $z = 4$ to 0.15 at $z = 1.5$, while the halo spin of the DM is rather constant in time. Recall that a constant λ is actually a growing j, as the normalization factor $R_v V_v$ is monotonically increasing in time. The growth in j is as qualitatively expected from TTT, and the faster growth for the cold gas largely emerges from the growth of the quadrupole moment of cold gas with respect to that of the DM in zone I, as seen in Fig. 3. While the spin of the cold gas in the halo is two-to-three times larger than that of the DM, the baryons within $0.1R_v$, dominated by stars that formed from previously accreted cold gas, show a spin parameter that is somewhat smaller than that of the halo DM, and rather constant in time. The reduction in the spin of the baryons is partly a result of the mixing with the baryons that entered the disc earlier with lower sAM, and partly due to AM loss in the inner halo.

We notice in Fig. 1 that the sAM profile for the cold gas is roughly $j(r) \propto r^{0.5}$ throughout zone II, crudely consistent with the profile expected from TTT with the AM roughly conserved during the streaming in. The tendency of the cold gas to preserve its sAM in zone II is indicated by noticing in the cold density maps shown in Fig. 2 that the streams in zone II tend to be straight lines, namely with

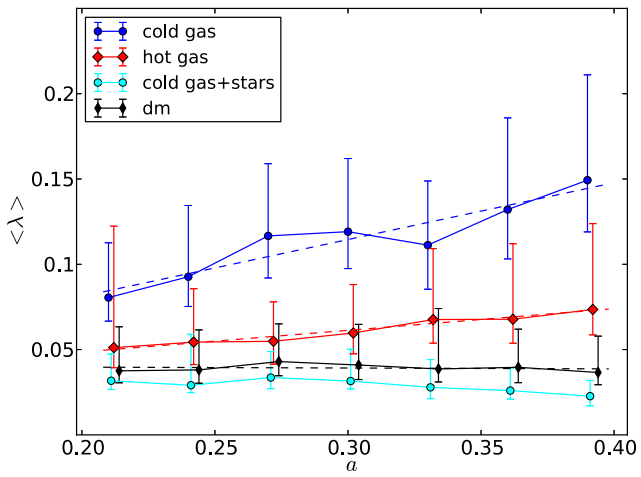

Figure 7. Evolution of the average spin parameter of different components within the virial radius. Cold gas (excluding the inner $0.1R_v$) (blue), hot gas (red), dark matter (black), and cold gas in the halo plus stars in $r < 0.1R_v$ (cyan). Shown are the mean and standard deviation over all haloes in bins that consist of three snapshots each. While the spin of the cold gas in the halo is higher than that of the dark matter by a factor of 2–3 and rising with time, the spin of the baryons in the galaxy is somewhat smaller than that of the halo dark matter and rather constant in time, due to mixing and AM exchanges within the inner halo and the disc, on zones III and IV. The best linear fit (dashed line) for the halo cold gas is $\lambda = 0.015 + 0.33a$, and for the hot gas $\lambda = 0.023 + 0.13a$.

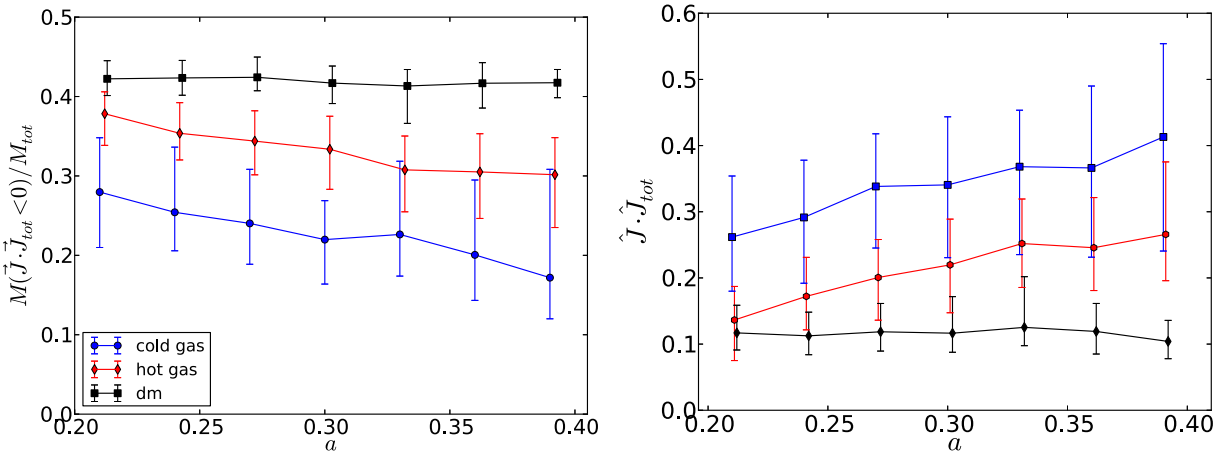

Figure 8. Coherence of AM in the different components within the virial radius, zone II. The quantities are mass-weighted averaged over grid cells or particles within $(0.1-1)R_{\rm v}$, and over all snapshots and haloes. The error bars refer to standard deviation. Left: the fraction of mass with negative AM in the direction of the total AM of that mass component, measuring incoherence. Right: the cosine of the angle between the AM of the given component and the total AM direction of that component, measuring coherence. The AM in the cold streams is significantly more coherent than that of the dark matter.

constant impact parameters. Combined with the roughly constant streaming velocity, which results from dissipation and Lyman α radiation from the streams (e.g. Goerdt et al. 2010), the sAM remains roughly constant. For the cold gas, the AM that has been generated in zone I is basically being transported by the streams through zone II into the inner halo, zone III. This will be addressed again in Sections 5.2 and 5.3, Figs 14 and 15.

4.3 Coherence of AM transport

It turns out that the difference between the AM properties of the different components within the halo cannot be attributed to systematic differences in the sAM amplitudes of individual gas cells or DM particles ($j = bv$ with b the impact parameter and v the speed) – these local sAM values for the different components are rather comparable. The main difference in zone II is in the coherence of the motions of the cold gas and in the AM transport efficiency.

Fig. 8 measures in two ways the level of coherence of the AM transported by the different components within $(0.1–1)R_{\rm v}$ as a function of time. The averages shown are over particles or over gas cells within each halo, and then averaged over all haloes. First is the mean fraction of mass with a negative contribution to the total AM of that component within the halo, which serves as a measure of deviations from coherence. We see that the DM has a large negative fraction, with an average slightly above 0.4 and constant in time. The cold gas has a much smaller negative fraction, decreasing from 0.28 at $z = 4$ to 0.18 at $z = 1.5$, thus indicating larger coherence. A second measure of coherency is the mean cosine of the angle between the AM in each cell and the total AM of that component. The DM has a low mean cosine at the level of 0.1, indicating strong incoherence. The mean for the cold gas is much larger, increasing from 0.27 at $z = 4$ to 0.41 at $z = 1.5$. Thus, these two measures confirm that the cold gas transports the AM in a coherent way, while there is significant mixing for the DM, and some mixing for the hot gas.

The coherence of the AM in the different components is demonstrated visually for two of our galaxies in Fig. 2. Recall that it shows maps of density and of positive sAM in the direction of the total AM of that component, thus distinguishing between the parts with positive and negative contributions. For the cold gas, the AM seems to be rather coherent within each stream throughout zone II, starting beyond $2R_{\rm v}$ and ending in the inner halo. On the other hand, the thick streams of DM are well defined only outside the virial radius and they become a rather messy mixture within $R_{\rm v}$, and each of them consists of positive and negative contributions to the net AM of the DM.

As found earlier (Danovich et al. 2012), Fig. 2 illustrates that in the two examples shown the mass is transported mainly by three streams. As for the AM, in galaxy MW1 it is transported pretty evenly and coherently by the two massive cold streams, with a small negative contribution from the less massive stream(s). In SFG1, most of the positive AM of the cold gas is transported by the single most massive stream, a second stream has a much smaller contribution in the same AM direction, and the third stream mostly carries AM of an opposite sign. Thus, the different cold streams can contribute positively or negatively to the net total AM that they bring in. Since the measures of coherence in Fig. 8 refer to all the cold streams together, they are contaminated by the large-scale incoherence between the streams and thus underestimate the coherence within each stream by itself. The counter-rotating streams can have very dramatic effects on the central galaxy (see Sections 5 and 6 below).

4.4 Torques on cold streams

We saw in Fig. 5 that the gravitational torques, with $q \sim 1$–2 in zone II, are apparently capable of making significant changes to the AM also in this region. However, this refers to the total amplitude of the torque in a thin shell, while the torque and its interplay with the AM of the shell can vary in direction from shell to shell, so the total net effect on the stream AM as it flows from outside $R_{\rm v}$ to the inner halo could be significantly smaller.

Fig. 9 shows the profiles of two components of the normalized torque q acting on shells of different radii r. Shown is the component parallel to $\hat{J}$, which changes the amplitude of the AM. Also shown is the perpendicular component that lies in the plane defined by $\hat{J}$ and $\hat{J}_{\rm disc}$, which measures the tendency for alignment with the disc AM (hereafter the 'alignment' component). The way the disc is defined is described at the beginning of Section 6. The profiles are shown for four individual galaxies and stacked over six galaxies (six snapshots). We see that the values of the components of q in

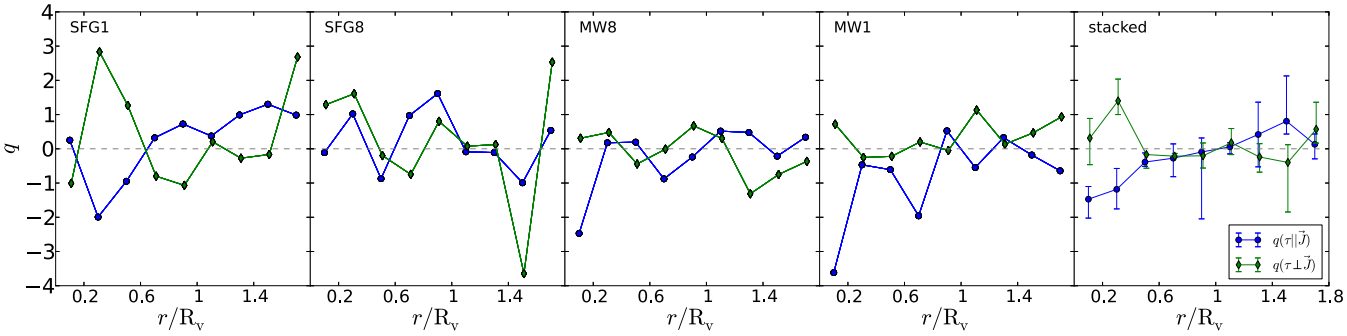

Figure 9. Profile of the torque acting on the cold gas in concentric shells, with respect to the AM in the same shell, $\boldsymbol{J}$. Shown are the component parallel to $\hat{J}$ (blue) and the component perpendicular to $\hat{J}$ in the plane defined by $\hat{J}$ and $\hat{J}_{\rm disc}$ (green). The former is associated with a change in AM amplitude and the latter refers to a tendency for alignment with the disc. Here $t_{\rm torq} = 0.5t_{\rm v}$. The profiles are shown for four individual galaxies, and the stacked profile are over six galaxies (MW1 $z = 1.63$, MW3 $z = 2.33$, MW8 $z = 2.33$, SFG1 $z = 3.17$, SFG8 $z = 2.17$, VL01 $z = 2.57$). Related quantities cell-by-cell are shown in Fig. 15. Dense clumps have been removed, to obtain smoother curves, but the trends at small radii remain. In the outer halo, zone II, the q values for individual galaxies can be of the order of unity but they fluctuate in sign, and the stacked q values there are lower than unity. In the inner halo, zone III, the parallel and alignment components tend to be negative and positive, respectively, at the level of $|q| \sim 1$, indicating a tendency for lowering the AM amplitude while aligning it with the disc AM.

the shells of zone II are of the order of unity, but in each individual galaxy the variation between radii is large such that the average q throughout zone II is smaller than unity. This is consistent with the evidence discussed above for only small changes in the AM in this zone, where the AM of the cold gas is being transported by the streams.

4.5 Hot gas

As seen in Fig. 6, the hot gas is a non-negligible component in the halo outside the galaxy, at $(0.1 - 1)R_{\rm v}$, where it constitutes 22 per cent of the baryons (28 per cent if the gas of intermediate temperatures slightly above 10^5 K is included) and 40 per cent (47 per cent) of the gas (see also Kereš et al. 2005, 2009, Dekel & Birnboim 2006, Birnboim, Dekel & Neistein 2007; Ocvirk et al. 2008; Agertz et al. 2009; Ceverino et al. 2010). This gas partly consists of infalling gas that has been heated by the virial shock and is now in quasi-static equilibrium within the halo, and partly of outflowing gas due to feedback. Its average spin parameter is $\langle\lambda_{\rm hot}\rangle = 0.061$, about half that of the cold gas in that region, and 42 per cent higher than that of the DM. The same is re-confirmed in Fig. 1, which emphasizes that the spin parameter of the hot gas shows a flatter increase with radius than the DM and the cold gas, converging to an sAM similar to that of the DM in zone I outside the halo. This indicates that a substantial fraction of the hot gas in the inner halo originates from the cold-stream gas that has been heated in the way in Nelson et al. (2013), e.g. by shocks within the supersonic streams and by their interaction with the hot CGM (Mandelker et al. in preparation). The mixing with hot outflows is expected to reduce the hot-gas spin as the outflows preferentially remove low-spin gas from the central dense star-forming regions.

5 PHASE III: AM LOSS DUE TO STRONG TORQUES IN AN EXTENDED RING

5.1 Structure of the extended ring

The third phase involves the cold gas in the inner halo and in the greater vicinity of the central disc, typically at $(0.1–0.3)R_{\rm v}$. The outer radius of this zone is determined by the impact parameter of the cold stream that dominates the AM. This region was termed 'the messy region' based on the visual impression of the complex structure and kinematics seen in simulations (Ceverino et al. 2010), or 'the AM sphere' based on the indications for AM exchange in this region deduced from the misalignment of the disc and the AM of gas in the outer halo (Danovich et al. 2012). Indeed, we will discuss below clear evidence for AM exchange in this zone. For example, we see in Fig. 6 that the average spin parameter of the cold gas at $r < 0.1R_{\rm v}$ is $\lambda = 0.039$. While this is comparable to the spin of the DM in the halo, it is smaller by a factor of 3 than the spin of the cold gas in the halo outside the disc. This could be partly because of mixing of the newly arriving high-sAM gas with the disc gas that arrived earlier with lower sAM, and partly due to AM loss by torques in the greater vicinity of the disc, which we will address below.

The cold-gas streams that flow in through zone II on roughly straight lines with impact parameters b dissipate kinetic energy near pericentre, at $r \sim b$, through interaction with the dense gas already there. This makes the streams bend towards more circular orbits about the disc. With a typical stream velocity of $1.3V_{\rm v}$, the stream with the largest impact parameter defines the outer boundary of this region at $b \sim \lambda_{\rm max}R_{\rm v}$, which is typically $0.3R_{\rm v}$. The incoming gas thus forms an extended outer ring at $(0.1–03)R_{\rm v}$. The ring is in general tilted with respect to the central disc because its incoming AM has been determined outside $R_{\rm v}$, and is in general not aligned with the disc (Danovich et al. 2012). As we demonstrate below, gravitational torques, exerted largely by the inner disc, make the gas in the extended ring lose AM and thus spiral in towards the inner disc, as it gradually aligns its AM with the spin axis of the inner disc. This typically takes less than an orbital time.

The large-scale structure of zone III is illustrated in Fig. 10, which shows images of the projected cold-gas distribution for four simulated galaxies with different masses at different redshifts. Shown are zoom-out views in boxes containing circles of radius $2R_{\rm v}$ and zoom-in views in boxes of radius $0.5R_{\rm v}$, with the circles of radius $0.3R_{\rm v}$ and $0.1R_{\rm v}$ marked. These projections are face-on in the disc frame, with the disc rotation clockwise, namely the AM pointing into the page. One can see that 2–5 streams are well defined in zone II, reaching zone III with detectable impact parameters, most of which indicate co-rotation with the disc but some are counter-rotating. Zone III is the interface between the incoming cold streams

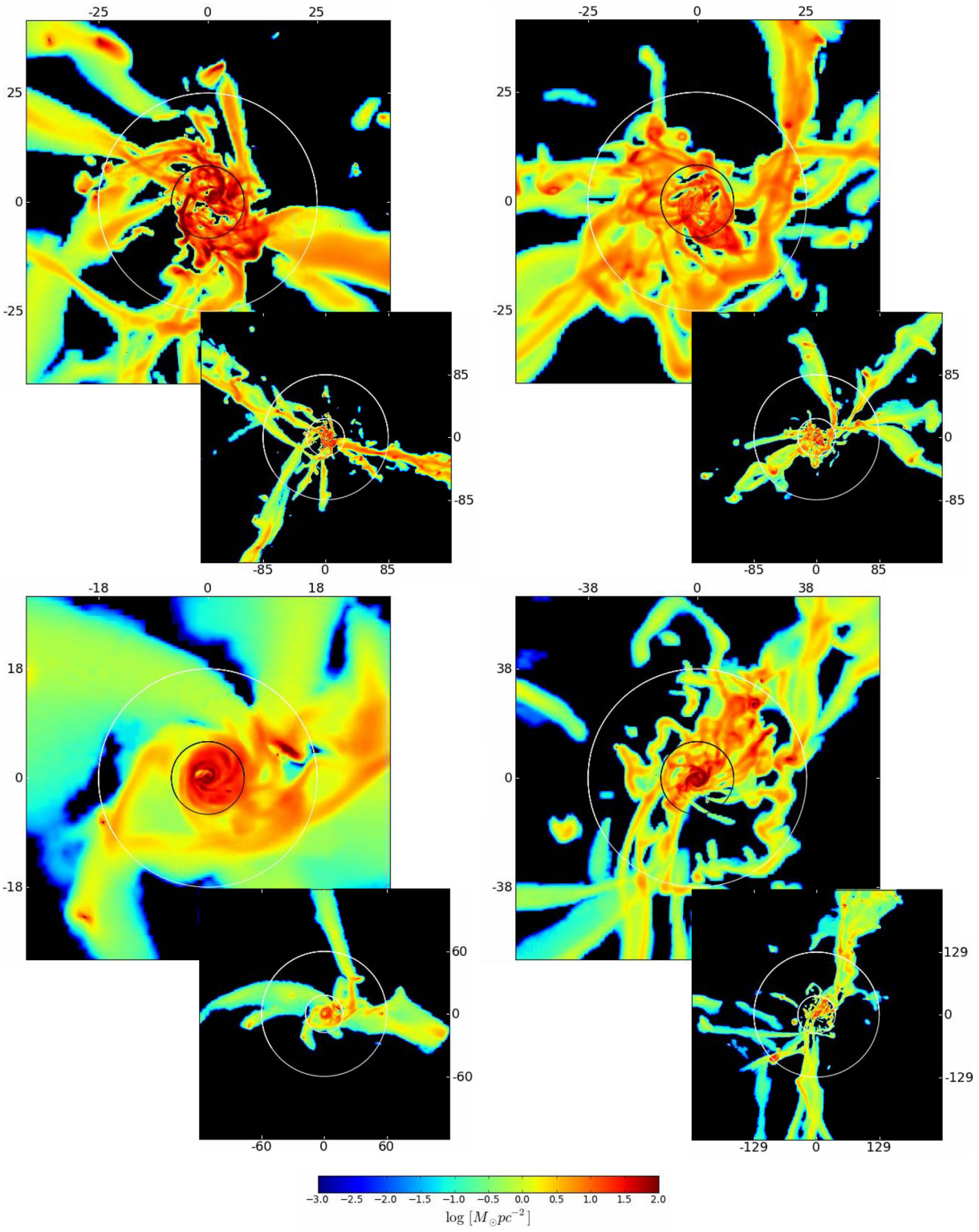

Figure 10. Density projections of the cold dense gas at the inner halo in four galaxies from Table 2 (SFG1 $z = 3.17$, SFG8 $z = 2.92$, MW8 $z = 2.33$, MW1 $z = 1.63$ from top-left to bottom-right). The projections of thickness R_v are face-on in the disc frame. In the small zoom-out views the box is of side $4R_v$ and the circles are of radii R_v and $0.3R_v$. In the zoom-in views, the box is of side $1R_v$ and the circles are of radii $0.3R_v$ and $0.1R_v$. The lengths on the box sides are in kpc. The interface region between streams and disc, zone III, shows a non-uniform, filamentary and clumpy 'ring' where the streams settle into a rotating pattern.

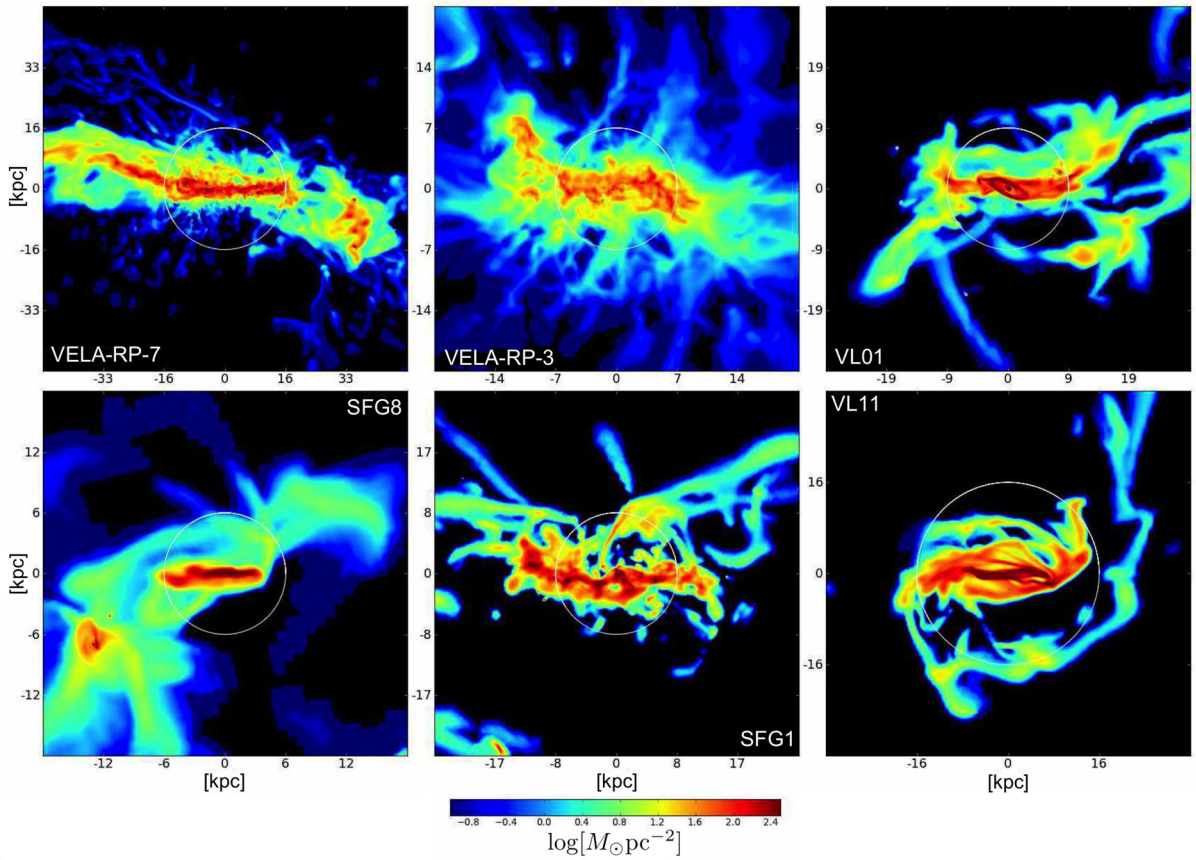

Figure 11. Projections of cold-gas density in edge-on directions of six discs from Table 2 (from top-left to bottom-right: VEL7 $z = 1.17$, VEL3 $z = 1.50$, VL01 $z = 2.45$, MW8 $z = 2.33$, SFG1 $z = 3.17$, VL11 $z = 1.50$). The box side and thickness are $0.3R_\mathrm{v}$. The circle marks $0.1R_\mathrm{v}$. These projections highlight the warps associated with the extended tilted ring. The pictures from the simulations with higher resolution and stronger feedback (two top-left panels) highlight the tilt of the outer ring, which in one extreme case extends out to beyond 30 kpc (VEL7).

and the inner more organized (though still perturbed) rotating disc. We see that the 'ring' in zone III is far from being a uniform ring, as the gas distribution shows large-scale deviations from circular symmetry involving a complex pattern of filaments and clumps that are reminiscent of the stream pattern in zone II. These four examples also illustrate that the extent of zone III indeed scales with the virial radius, typically at $0.3R_\mathrm{v}$, which implies in turn that it is increasing with mass and growing in time.

Fig. 11 shows projections of cold-gas density in the edge-on direction of the disc in six example galaxies from our sample, highlighting the tilt of the extended ring, which appears as pronounced extended warps. Fig. 12 shows another type of images of the density of cold gas within zone III in four simulated galaxies. These images were produced using the IFrIT visualization tool. Each gas cell is treated as a particle and coloured according to the gas density in the cell. By an optimal selection of opacities for the different colours and viewing directions, the images attempt to give a certain three-dimensional impression of the nature of the extended ring and its relation to the inner disc. These images indicate that the gas streams in the ring spiral in over less than one circular orbit. This is confirmed in Fig. 13 that presents streamlines in the same region for one of the galaxies. The streamlines were generated from one snapshot by interpolation between the velocities in grid cells. The streamlines show how the streams bend and gradually join the inner rotating disc, like a stream of cars entering an expressway (coined 'on-ramp' by Kereš et al. 2005).

5.2 Kinematics of the extended ring

Fig. 14 shows the distributions of several quantities of interest as a function of radius r/R_v for each of the four galaxies shown in Fig. 10 and for the four galaxies stacked together (right-hand column). Each grid cell is represented by a point coloured by log mass of cold gas and the dark line marks the mass-weighted average at the given radius. We note that in these pictures elongated horizontal features may refer to coherent streams, while vertical spikes may be associated with clumps.

The upper row refers to the ratio of tangential to radial components of the velocity V_tan/V_r. We see that at large radii, in zones II and I, this ratio is typically below unity, indicating rather radial inflow, except for spikes that represent rotating satellite clumps with high V_tan. In the inner halo, the ratio is increasing towards the centre, with the average above unity at $r < (0.3 - 0.6)R_\mathrm{v}$, indicating an increasing tendency for circular motion in zone III.

The second row in Fig. 14 is the impact parameter of the cold gas. It is computed using $b = |\boldsymbol{r} \times \hat{v}|$, where $\boldsymbol{r}$ is the position vector of the gas cell and $\hat{v}$ is the unit vector in the direction of the total velocity of the gas cell. The impact parameter is defined as positive or negative depending on the orientation of each cell's AM vector with respect to the disc AM vector. In this case, the dark line is the mass-weighted average of the absolute value of the impact parameter. The average tends to be rather flat or slowly declining with decreasing radius in the outer halo, zone II, following a dominant stream that is represented by a horizontal concentration of red

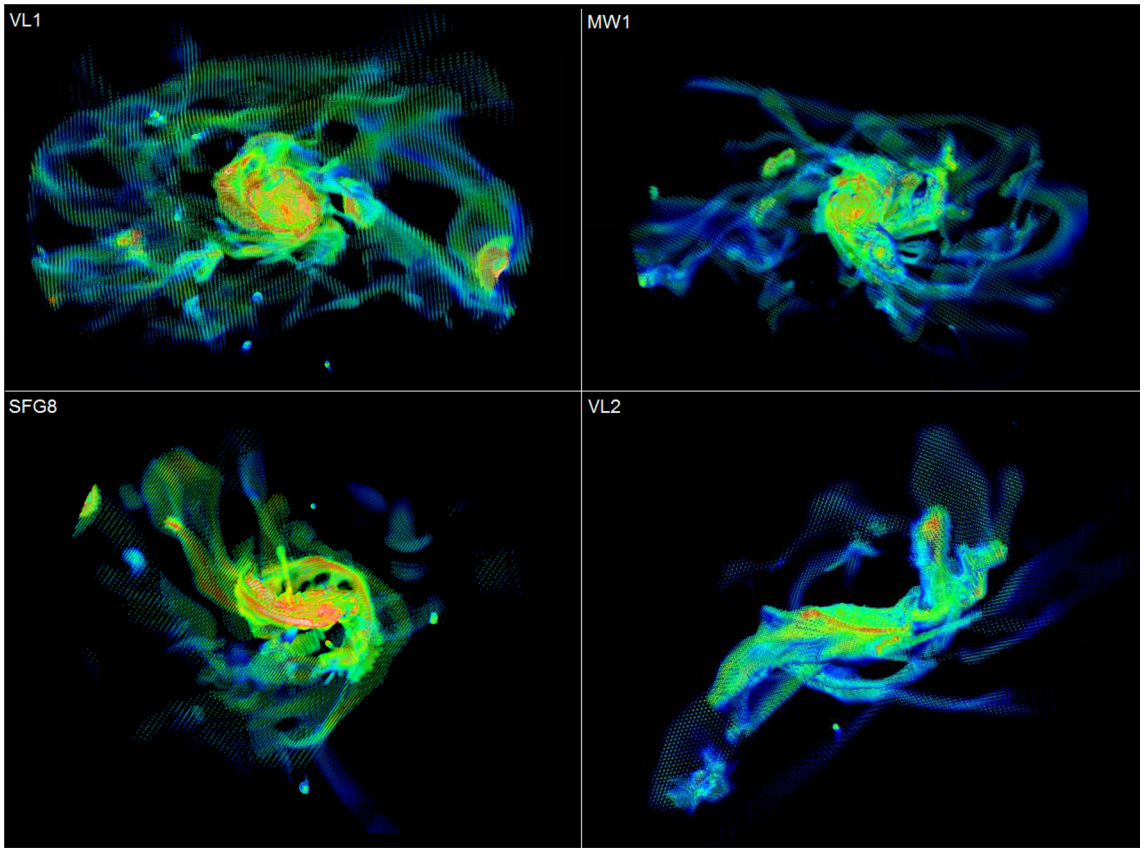

Figure 12. The extended cold-gas ring in four galaxies from Table 2 (VL01 $z = 2.57$, MW1 $z = 1.5$, SFG8 $z = 2.17$ and VL02 $z = 1.33$). The box side is $\pm 0.35 R_{\rm v}$. The cold-gas density within the greater disc vicinity shows the inner disc and the surrounding ring, where the gas streams bend, spiral in over less than one circular orbit, and smoothly merge with the disc.

Figure 13. Streamlines of gas in the inner halo of MW3 $z = 2.33$. The box side is about 30 kpc. The streamlines illustrate how the inflowing streams bend and merge smoothly into the inner rotating disc through an extended tilted ring.

points. In zone III, the average curve following the dominant stream is declining linearly with decreasing radius, close to the boundary that refers to circular motion, $b = r$. The outer radius of zone III is well defined in these plots.

We can also see in the second row of Fig. 14 that while most of the gas mass tends to be corotating with the disc, there is a significant fraction that is counter-rotating, with a negative impact parameter, originating from counter-rotating streams. We find that on average about 30 per cent of the instreaming gas mass in the inner halo, (0.1–0.3)$R_{\rm v}$, is counter-rotating with respect to the net instreaming AM in the same volume. This component carries a negative contribution with an amplitude that is on average 43 per cent of the positive component, namely 75 per cent of the net total inflowing AM. The counter rotation can thus have very important effects on the outer ring and on the inner disc (see Section 6).

The third row of Fig. 14 shows the sAM of the cold gas, normalized as a spin parameter λ. The smooth blue line is an estimate of the maximum λ possible for particles in circular orbits at the given radius under the assumption that the mass distribution is spheri-symmetric. We see that the mean is below the maximum for circular orbits, but there is some gas slightly above the limit, indicating deviations from spherical symmetry. The steep decline of the

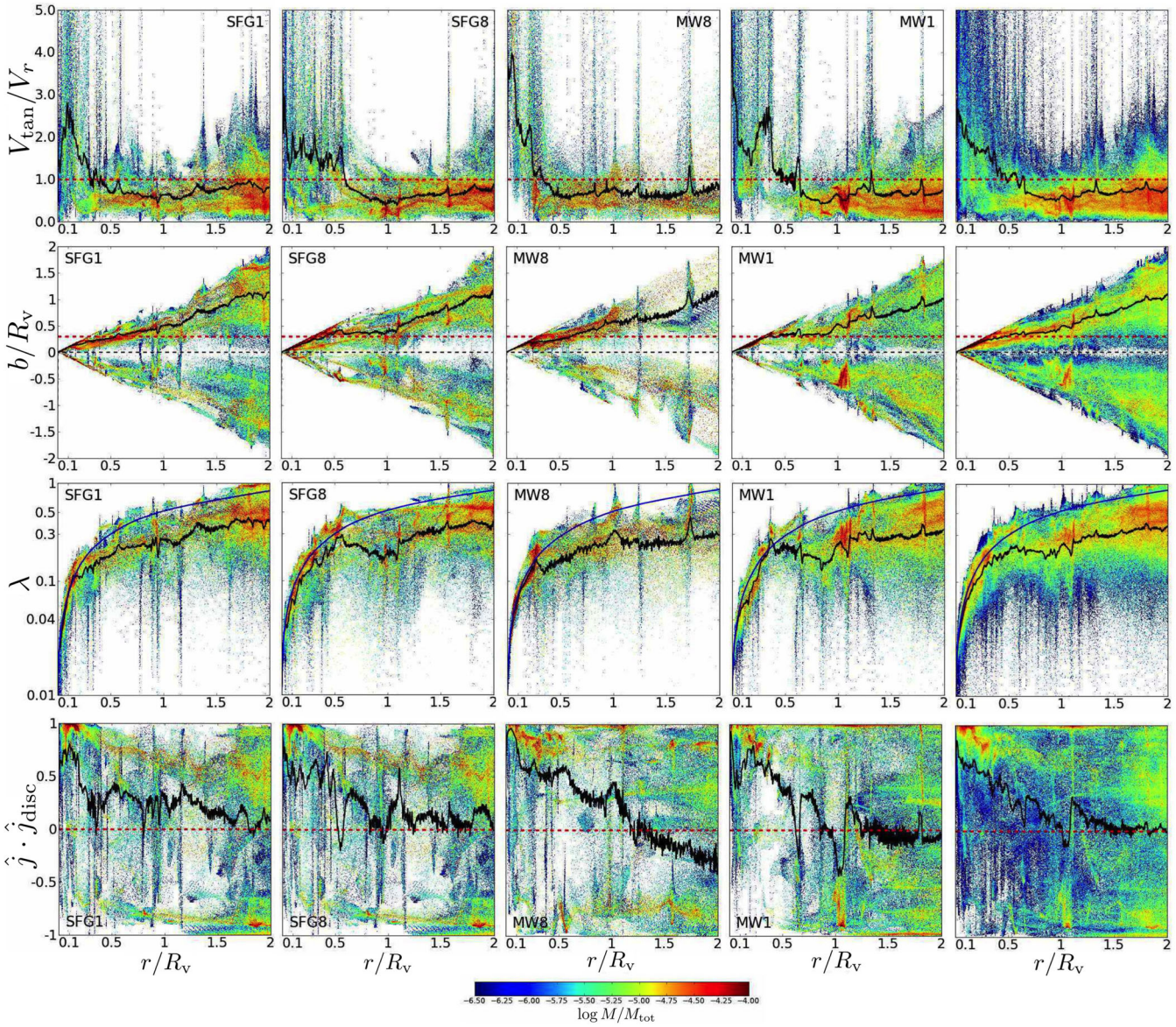

Figure 14. Kinematics in zones II and III. Shown are 2D histograms for four galaxies and stacked (right-hand column), referring to the following parameters for the cold gas as a function of radius Top: tangential to radial velocity ratio $V_{\rm tan}/V_r$. Second row: impact parameter $b/R_{\rm v}$ (the red-dashed line marks $0.3R_{\rm v}$). Third row: spin parameter λ (the blue line marks $(GM(<r)r)^{1/2}$). Bottom: alignment of the AM with the disc AM $\hat{J}\cdot\hat{J}_{disc}$. The colour corresponds to the log of the mass in each pixel. The black line is the mass weighted mean at r. The snapshots from Table 2 are SFG1 $z = 3.17$, SFG8 $z = 2.92$, MW8 $z = 2.33$, and MW1 $z = 1.63$. The outer halo in zone II is characterized by motions with a dominant radial component, a rather constant impact parameter, a high spin parameter and an AM direction that is poorly correlated with the disc AM. At gradually smaller radii in the inner halo, zone III, one can see an increasing circular velocity component, a declining impact parameter associated with spiralling in, a declining spin parameter associated with AM loss, and an increasing alignment with the inner disc.

average curve in zone III, following most of the mass, is gradually approaching the boundary for circular orbits.

The bottom row of Fig. 14 shows the cosine of the angle between the cold-gas AM and the disc spin axis, with unity corresponding to perfect alignment. Horizontal filaments of concentrated red points refer to streams. The average shows poor alignment in zone II, with the cosine smaller than 0.4, implying uncorrelated orientations for the stream AM and the disc AM (as found in Danovich et al. 2012). There is a marked increase in the alignment with the inner disc in zone III, from below 0.4 to 0.7–0.9. The streams with misaligned AM seen in zone II either tend towards alignment or disappear in zone III.

5.3 Torques in the ring

The gas reaching zone III with a non-negligible impact parameter and the correspondingly high AM needs to lose AM in order to spiral in and change its direction for alignment with the inner disc. We saw in Figs 4 and 5 that the gravitational torques dominate the AM exchange. In zone III, they should be strong torques, exerted locally, presumably mostly by the inner disc, and possibly by dynamical friction.

Fig. 15 shows the distributions of the torque components parallel and perpendicular to the local AM vector of the cold gas in grid cells, as a function of radius. It is to be compared to Fig. 9, which refers to the torque components acting on the cold gas averaged

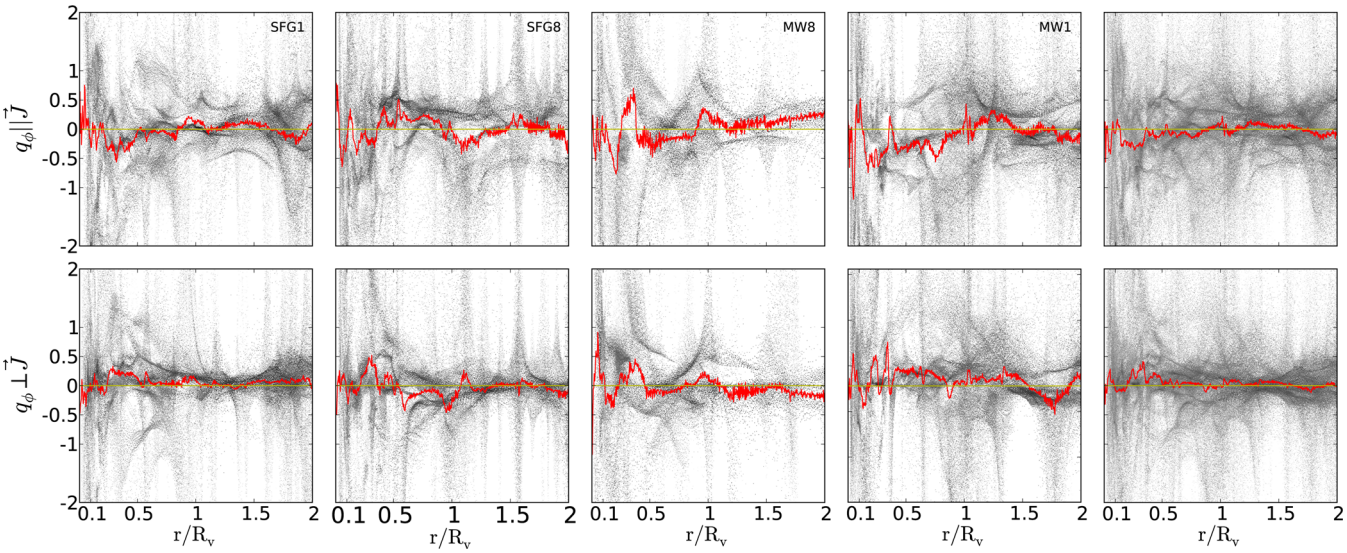

Figure 15. Radial profiles of normalized torques for the four galaxies shown in Fig. 14 and stacked (right-hand column). Top: the torque parameter component in the direction of the AM of each cold-gas cell, emphasizing the effect of the torque on the amplitude of the AM. Bottom: the torque parameter component in the direction perpendicular to the AM vector of each cold-gas cell $\boldsymbol{J}$ and in the plane defined by $\boldsymbol{J}$ and the disc AM, measuring the tendency towards alignment with the disc. The torques are ineffective in zone II, while in zone III they are capable of lowering the AM amplitude and increasing its alignment with the disc AM. These features are common to most galaxies in our sample.

over shells with respect to the AM in the shell. Four panels refer to the four galaxies shown in Fig. 14 and the right row shows the stacked distributions. The sign of the parallel torque indicates whether it acts to increase or decrease the AM in that cell. The time assumed here for q in equation (10) is $t_{\rm torq} = 0.2t_{\rm v}$, a characteristic crossing time for zone III. This serves as a lower limit for the actual time available for the torques to act during the spiralling in of the streams in the ring. The vertical features of high density of points correspond to neighbourhoods of satellite clumps, where the force is directed towards the clump centre but the radius vector is measured with respect to the galaxy at the halo centre. Horizontal features correspond to streams. In the outer halo, zone II, the average parallel component is typically much smaller than unity. In the inner region, there is a tendency for the parallel component to become negative, namely acting to reduce the AM amplitude in each cell. The horizontal filaments seen in zone II tend to bend towards negative values upon entry to zone III, indicating streams that are being increasingly torqued in the inner region.

The time-scale for spiralling in of the extended ring is the time-scale for a change of the order of unity in the AM magnitude, namely $t_\tau \sim |q_\parallel|^{-1} t_{\rm torq}$. With $q_\parallel \sim -0.3$ and $t_{\rm torq} = 0.2t_{\rm v}$ in Fig. 15, this is $t_\tau \sim 0.6t_{\rm v}$, namely of the order of the characteristic orbital time in zone III. A similar conclusion can be obtained from the torque profiles shown in Fig. 9, where in zone III $q_\parallel \sim -1$ and where $t_{\rm torq} = 0.5t_{\rm v}$, so $t_\tau \sim 0.5t_{\rm v}$. This is consistent with the visual impression from Figs 12 and 13.

The bottom panels of Fig. 15 show the perpendicular component of q with respect to the local AM $\boldsymbol{J}$, chosen in the plane defined by $\hat{J}$ and $\hat{J}_{\rm disc}$, thus measuring the torque that tends to change the alignment of the local AM with the disc AM (see Section 6). In the outer halo, the alignment torque is typically rather small, consistent with what we saw in Fig. 9. In the inner halo, it shows larger fluctuations that on average are positive, namely, they act to align the outer ring with the inner disc, as seen in Fig. 14. A similar tendency for alignment is seen in the torque profiles shown in Fig. 9, where in zone III the perpendicular torque is $q_\perp \sim +1$.

5.4 On the origin of the torques

The AM exchange in the ring in zone III may largely arise from the gravitational torques exerted by the inner disc. To explore this possibility, we appeal to a simple toy model consisting of a uniform axisymmetric disc with radius R and mass M about an origin in the x–y plane. The gravitational potential generated by the disc at a point (r, θ), expanded to its monopole and quadrupole terms, is

$$\phi(r,\theta) = -\frac{GM}{r} + \frac{\alpha G M R^2}{r^3} P_2(\cos\theta) + O\left(\frac{R^4}{r^5}\right), \qquad (11)$$

where θ is the spherical polar angle measured from the z-axis, α is a numerical factor, and $P_2(x) = (3x^2 - 1)/2$ is the second Legendre polynomial. The monopole and quadrupole terms are sufficient for a good approximation far enough from the disc. The only contribution of the force $\boldsymbol{F} = -\nabla\phi$ to the torque is through its polar-angle component $F_\theta = -r^{-1}\partial\phi/\partial\theta$. The resulting torque, acting in the azimuthal direction ($\hat{\varphi}$), is

$$\tau_\varphi = rF_\theta \propto \frac{\alpha G M R^2}{r^3} \cos\theta \sin\theta\,. \qquad (12)$$

The torque component in an edge-on direction, e.g. the Cartesian direction x in the disc plane, is

$$\tau_x = \tau_\varphi \cdot (-\sin\varphi) \propto -\frac{\alpha G M R^2}{r^3} \cos\theta \sin\theta \sin\varphi\,. \qquad (13)$$

Fig. 16 shows the resulting pattern of the amplitude of this torque τ_x as viewed edge-on (namely projected in the y–z plane). The quadrupolar pattern, with alternating signs in the borders between quadrants where the torque reverses its direction, is very characteristic.

From this simplified analysis, we learn that the torques due to an axisymmetric disc do not affect the AM component parallel to the disc axis of symmetry. It tends to add an AM component in a direction perpendicular to the disc axis, inducing rotation in a plane perpendicular to the disc (namely about an axis that lies in the disc plane), and thus moving mass towards the disc plane. In

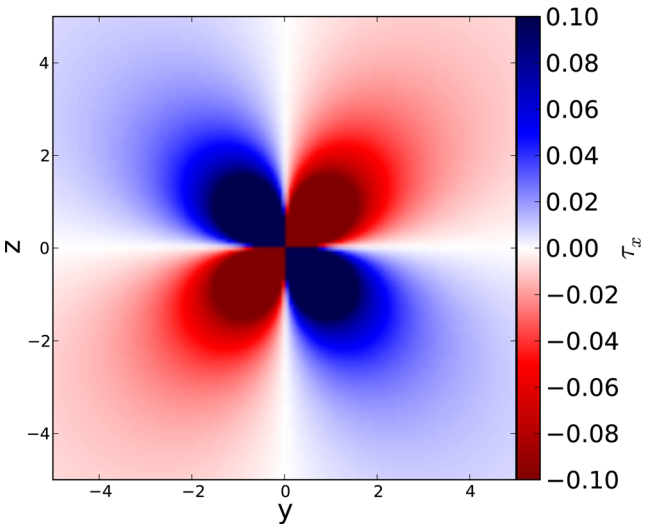

Figure 16. Gravitational torques exerted by an idealized uniform axisymmetric disc. The disc is in the x–y plane with its axis of symmetry along the z-axis. The map shows the x component of the torque (pointing out of the paper) in the $x = 0$ plane, perpendicular to the disc plane through its centre. The values of G and the disc radius and mass are set to unity. The torque shows a characteristic quadrupole pattern. The z component of the torque vanishes.

the case of an extended outer ring that is tilted with respect to the inner disc, the inner disc applies torques perpendicular to the AM of the ring particles, which results in a precession of their AM vectors. Being composed of collisional gas, the differential precession in the extended ring is associated with dissipation, which causes the outer ring to gradually align itself with the inner disc. We learn that the torques exerted by the inner disc work in general to align the ring and the disc. As long as they are not yet aligned, namely in the outer parts of zone III, these torques can also reduce the AM amplitude and induce the spiralling in of the extended ring.

Fig. 17 shows maps of gas density and torque magnitude in directions face-on and edge-on with respect to the discs in three simulated galaxies. The edge-on projections show a quadrupolar pattern that is rather similar to the pattern shown in Fig. 16 for the idealized case where the source is a pure disc. This is consistent with the conjecture that the inner disc is an important source of torque in zone III, with a significant contribution to the reorientation of the instreaming outer ring. However, the face-on projections also show a non-vanishing torque component along the disc axis of symmetry, which indicates that the source of the torque in zone III deviates from a pure disc. This is not surprising given that the high-redshift discs are very turbulent and perturbed, undergoing VDI and frequent mergers, and given the complex structure in zone III itself.

5.5 Observing the extended ring

We find that the rotating ring-like structure typically extends to $0.3R_{\rm v}$, e.g. about 30 kpc for massive galaxies at $z \sim 2$, and its radius scales with the virial radius. This is a refinement of earlier results (based on a few simulations with lower resolution) that indicated a somewhat more extended rotating pattern filling a large fraction of the halo (Stewart et al. 2011, 2013). We find that the cold gas in the outer halo is predominantly flowing in along rather straight coherent streams, with a certain tangential velocity component associated with the impact parameter of the stream.

The extended ring tends to be tilted relative to the disc plane, with the tilt increasing with radius. The mean tilt angle between the disc and the spin axis of the cold dense gas at $r = (0.1\text{–}0.3)R_{\rm v}$ is found to be $\sim 47^\circ$, namely largely uncorrelated with the orientation of the inner disc.

The internal structure of the extended ring is expected to be filamentary and clumpy, with the cold gas actually occupying only a fraction of the disc area. Fig. 18 shows an estimate of the cumulative distribution of H I column density along random lines of sight through the extended ring, at projected radii in the range $(0.1\text{–}0.3)R_{\rm v}$, stacked for all snapshots in the sample. Following Goerdt et al. (2012), the H I gas is crudely approximated by the cold gas below $1.5 \times 10^4 K$, with upper and lower limits provided by $T < 10^4$ K and $T < 2 \times 10^4$ K, respectively. A threshold density of $n > 0.01$ H cm^{-3} is applied in order to crudely select cells that are expected to be shielded against ionizing radiation (justified based on fig. 2 of Goerdt et al. 2012). Following the division into different column density classes in Fumagalli et al. (2011), we see that $\sim$30 per cent of the lines of sight are observable as damped Lyman α absorbers ($N_{\rm H\,I} > 10^{20.3}$ H cm^{-2}). Then $\sim$11 per cent are Super Lyman-limit systems ($N_{\rm H\,I} = 10^{19}$–$10^{20.3}$ H cm^{-2}), and less than a percent are Lyman-limit systems ($N_{\rm H\,I} = 10^{17.2}$–10^{19} H cm^{-2}). About 58 per cent of the lines of sight have H I column densities below 10^{17} H cm^{-2}, most of which are totally devoid of H I in our simulations.

The metallicity of the cold dense gas within $r = (0.1\text{–}0.3)R_{\rm v}$ averaged over all galaxies and snapshots is about $Z \simeq 0.1$ solar. This is in the ball park of the observed metallicities in damped Lyman α systems (Fumagalli et al. 2014).

Our results concerning the detectability of the outer ring should be regarded as a preliminary proof of concept. The detectability may depend on mass and on redshift, and may be affected by different levels of feedback. Our analysis here is rather simplified, not involving proper radiative transport (unlike, e.g. Fumagalli et al. 2011). By limiting the analysis to dense, self-shielded gas, we may miss the contribution of ionized gas to Lyman-limit systems. We defer detailed predictions for the observability of the outer ring to future work.

6 PHASE IV: AM EVOLUTION IN THE INNER DISC

6.1 Spin in the galaxy: VDI and feedback

Phase IV involves final adjustments of the AM within the inner disc. Processes responsible for substantial changes in the AM are feedback and VDI. Here, we only discuss these in a qualitative way, deferring a more quantitative analysis of the AM evolution in the disc to another paper.

Fig. 19 shows the probability distribution of the spin parameter for the baryons, cold gas and stars within the whole galaxy, the disc and the bulge components. Following Mandelker et al. (2014), the disc is confined to a cylinder of height ± 1 kpc and radius $R_{\rm d}$ (listed in Table 1) that encompasses 85 per cent of the gas mass out to $0.15R_{\rm v}$. The disc is also selected kinematically to consist of gas cells or stellar particles for which $j_z \geq 0.8\, r\, v$, where r is the radial distance from the centre and v is the cell or particle speed. This limits the disc cells or particles to those where the sAM component perpendicular to the disc is larger than 80 per cent of the maximum possible for the given energy at the particle position.

We see that the mean spin parameter of the gas disc is $\lambda_{\rm cold} = 0.040$, higher than that of the stellar disc, $\lambda_{\rm stars} = 0.019$.

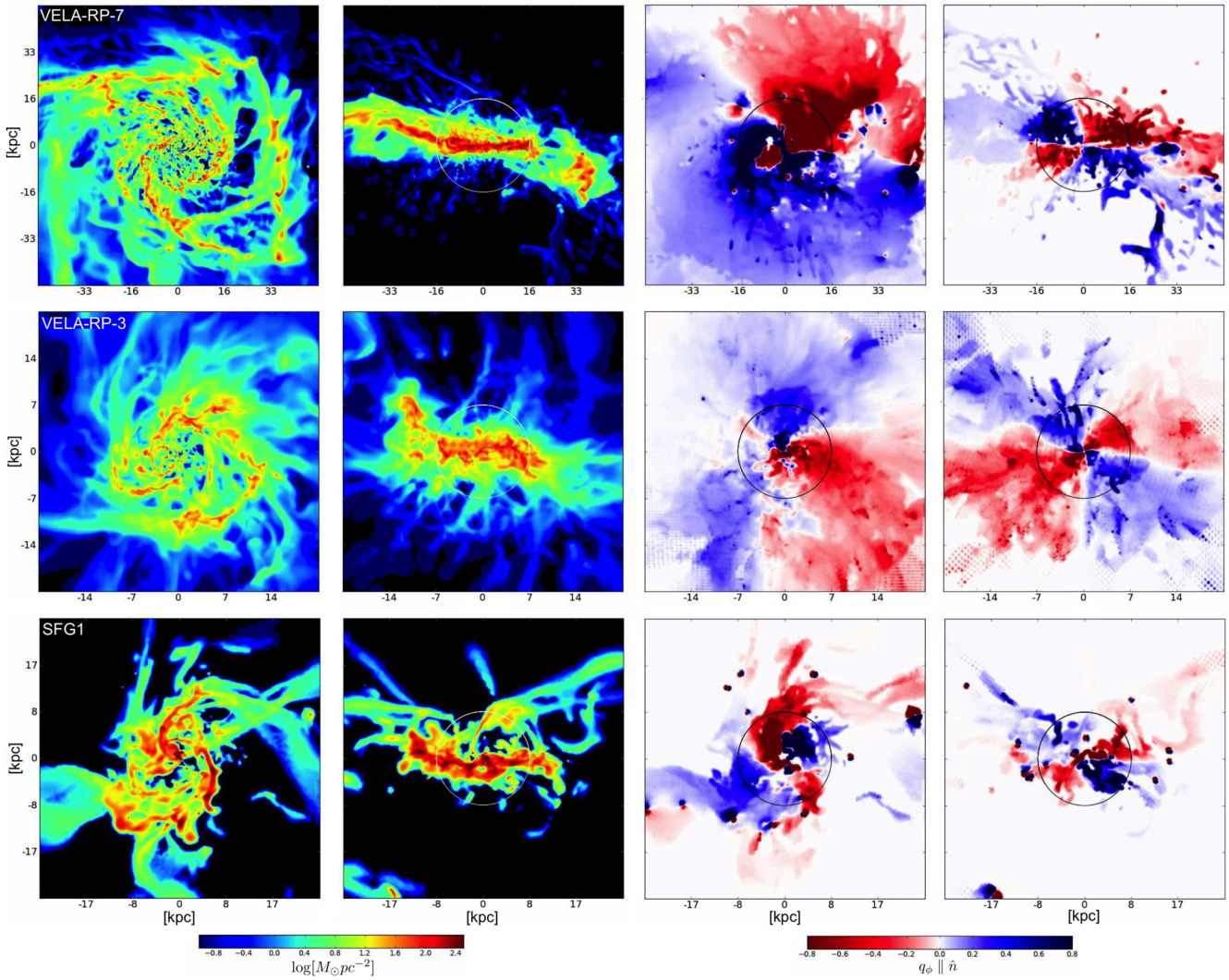

Figure 17. Torques in the greater disc vicinity, zone III. Shown for the cold gas in three galaxies (VEL7 $z = 1.17$, VEL3 $z = 1.50$, SFG1 $z = 3.17$) are face-on and edge-on projected density maps (left-hand columns), and the corresponding normalized torque component perpendicular to the plane shown, with $t_{\rm torq} = 0.2t_{\rm v}$ (right-hand columns). The box side is $0.6R_{\rm v}$ and the thickness of the slice is $0.3R_{\rm v}$. The circle marks $0.1R_{\rm v}$. In the edge-on views the torque shows a pattern that bears resemblance to the quadrupole pattern produced by an idealized disc, Fig. 16, but strong torques are also seen in the z-direction, indicating deviations of the torque source from an idealized disc.

The spin of the baryons (gas and stars) in the disc is naturally in between, $\lambda_{\rm bar} = 0.025$, closer to the stellar disc that constitutes ∼70 per cent of the mass. These disc spins underestimate the spins obtained in simulations with stronger feedback by ∼33 per cent (see Section 7).

The spin parameter of the disc is thus lower than that of the cold gas in the halo by a factor of 3–4, consistent with substantial AM loss by torques in zone III, as discussed in Section 5. It is interesting to note that the disc spin is comparable to and somewhat smaller than that of the DM in the halo (see e.g. Dutton & van den Bosch 2012). This result is not very different from the result obtained by the simplistic cylindrical contraction model despite the very different AM evolution tracks for the cold gas and for the DM, as discussed in the current paper. This is good news for semi-analytic model of galaxy formation, which commonly adopt the disc sizes based on the simplistic model.

It can be seen in Fig. 19 that, unlike the other components in the galaxy and in the halo, the distribution of λ for the gas disc is better fit by a Gaussian than by a lognormal distribution.

The sAM of the gas disc is expected to be larger than that of the stellar disc for two reasons. First, the gas is a more direct tracer of the recently arrived mass, which is expected to come in with a higher sAM, while the stars are made of baryons that arrived earlier with lower sAM. Secondly, the gas that arrived earlier was subject to outflows generated by stellar, supernova and active galactic nucleus (AGN) feedback. These mechanisms preferentially remove gas from the dense central regions where the SFR is high and the AGN activity takes place, and therefore the outflows tend to increase the effective sAM of the remaining gas in the disc (e.g. Maller & Dekel 2002; Governato et al. 2010; Brook et al. 2011; Brooks et al. 2011; Guedes et al. 2011).

The high-redshift massive discs with high gas surface density undergo VDI, in which the discs develop large-scale elongated transient perturbations and small-scale giant clumps. These perturbations exert mutual torques, which preferentially drive AM out carried by a small fraction of the disc mass. In response, most of the disc mass flows in, as clump migration and as off-clump gas inflow. This leads to the formation of a central bulge of relatively low AM.

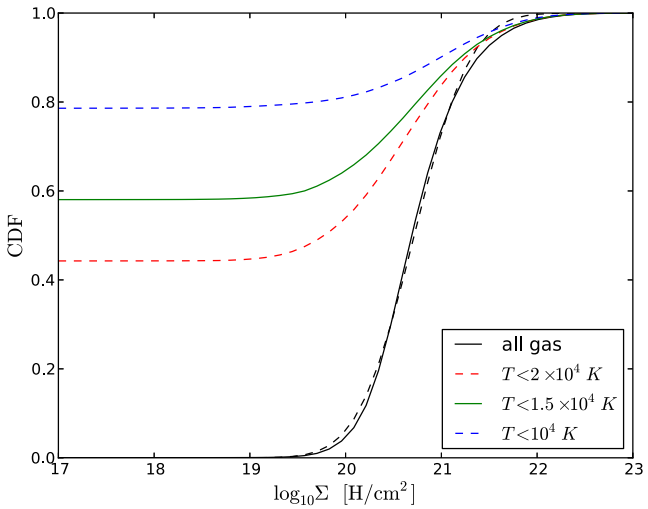

Figure 18. Cumulative distributions (CDF) of the H I column density along random lines of sight through the extended ring, averaged over all snapshots of all galaxies. Each of 400 lines of sight has a circular aperture of radius 300 pc. The lines of sight are chosen at random orientations and with random points of intersection with the ring at projected radii in the range $(0.1–0.3)R_{\rm v}$, averaged over all snapshots in the sample of simulations. The H I gas is crudely approximated by all gas with $n > 0.01 {\rm H\,cm^{-3}}$ and $T < 1.5 \times 10^4$ K (green), with upper and lower limits provided by $T < 10^4$ K (dashed blue) and $T < 1.5 \times 10^4$ K (dashed red), respectively. The CDF of all the gas is shown for reference (black) and fitted by a Gaussian PDF (dashed black). While about 58 per cent of the lines of sight are of low H I column densities, about 30 per cent are above a column density of $2 \times 10^{20} {\rm H\,cm^{-2}}$ and are thus observable as damped-Lyman α systems.

The time-scale for inflow is of the order of one or two disc orbital times (Dekel et al. 2009, 2013). It has been argued by Dekel & Burkert (2014) that the original spin parameter of the gas disc, which determines the initial gas surface density in the disc, determines whether the gas inflow rate is faster or slower than the SFR. If the spin is relatively low, then the gas fraction is high, the inflow is faster than the SFR, it is gaseous and dissipative, and it leads to compaction into a gas-rich, high-SFR 'blue nugget'. If the spin is relatively high, then the gas fraction is lower, the SFR is faster, and the result is a more extended stellar disc. This is expected to lead to a bi-modal distribution of star-forming galaxies, the extended clumpy discs and the compact blue nuggets, with the latter more frequent at higher redshifts. The extended discs had more AM to begin with, and have not lost much during their VDI phase, so they are expected to be of high AM. The blue nuggets had less AM initially, and have lost much of it during compaction, being carried away by an outer, co-planar, gaseous and star-forming ring (Genzel et al. 2013; Zolotov et al. 2014), not to be confused with the tilted extended ring at larger radii discussed in Section 5. However, feedback is likely to remove more low-AM central gas from the nuggets, thus partly compensating for the AM loss and bringing the mean sAM up.

The final disc spin parameter in phase IV is sensitive to the strength of the feedback processes. We briefly mention in the next section preliminary estimates that indicate an increase of ∼50 per cent in the spin of the inner disc when stronger feedback is incorporated, while the effects on the outer ring and gas in the halo and outside it are much smaller.

6.2 Counter rotation

We saw in Section 5 that the amplitude of the counter-rotating component of the instreaming gas in $(0.1 - 0.3)R_{\rm v}$ is ∼75 per cent of the amplitude of the net AM of that component. In order to evaluate the effect of the counter-rotating streams on the disc, we measure J_-, the AM component in the direction antiparallel to the disc AM, for the instreaming gas at radial distances and velocities that will bring it to the disc in less than an outer-disc orbital time. This time is typically $t_{\rm orb} \sim 250$ Myr in our galaxies at $z \sim 2$, involving most of the instreaming gas at $0.1–0.5R_{\rm v}$. For the galaxies at $z = 2–3$, the median of $J_-/J_{\rm d}$ (where $J_{\rm d}$ is the AM of the gas disc) is about 10 per cent, but about 20 per cent of the galaxies have $J_-/J_{\rm d} \sim 1$. Indeed, in a period of 250 Myr, about 15–20 per cent of the discs flip their orientations, namely change their spin direction by more than 90°. This substantial fraction of counter rotation can affect the galaxy in several different ways. The gaseous streams can be important in stimulating the VDI in high-redshift galaxies, which seems to be non-linear with a Toomre parameter significantly above unity (Inoue et al. in preparation). In turn, it can trigger a dramatic wet compaction event into a compact star-forming 'blue nugget', followed by quenching to a compact 'red nugget' that eventually makes the core of an elliptical galaxy (Dekel & Burkert 2014; Zolotov et al. 2014). Indeed, our simulations indicate that the frequency of spin flips is suspiciously similar to the fraction of galaxies that start their compaction event in a similar period.

Alternatively, the stellar component of the streams could lead to the formation of a stellar disc with two counter-rotating components relative to each other, as observed and as analysed in simulations (Algorry et al. 2013).

7 POSSIBLE EFFECTS OF STRONGER FEEDBACK

7.1 Simulations with different feedback strength

The simulations used here are state-of-the-art in terms of high-resolution AMR hydrodynamics and the treatment of key physical processes at the subgrid level. In particular, they properly trace the cosmological streams that feed galaxies at high redshift, including mergers and smooth flows, and they resolve the VDI that governs the high-z disc evolution and plays an important role in bulge formation (Ceverino et al. 2010, 2012, 2014b; Mandelker et al. 2014). The AMR code is superior to the common SPH codes for properly tracing some of the high-resolution hydrodynamical processes involved (e.g. Agertz et al. 2007; Bauer & Springel 2012; Scannapieco et al. 2012), and it seems to be comparable in its performance to new codes using a moving unstructured grid (Bauer & Springel 2012). However, like other simulations, the current simulations are not yet doing the most accurate possible job in treating the star formation and feedback processes. For example, the code used here assumes a somewhat high SFR efficiency per free-fall time, it does not follow in detail the formation of molecules and the effect of metallicity on SFR (Krumholz & Dekel 2012), and it does not explicitly include radiative stellar feedback (Krumholz & Dekel 2010; Murray, Quataert & Thompson 2010; Hopkins et al. 2012; Dekel & Krumholz 2013) or AGN feedback (Silk & Rees 1998; Hopkins et al. 2006; Ciotti & Ostriker 2007; Booth & Schaye 2009; Cattaneo et al. 2009; Fabian 2012; DeGraf et al. 2014). Therefore, the early SFR is overestimated, while the suppression of SFR in small galaxies is underestimated, resulting in excessive early star formation prior to $z \sim 3$, by a factor of the order of 2. As a result,

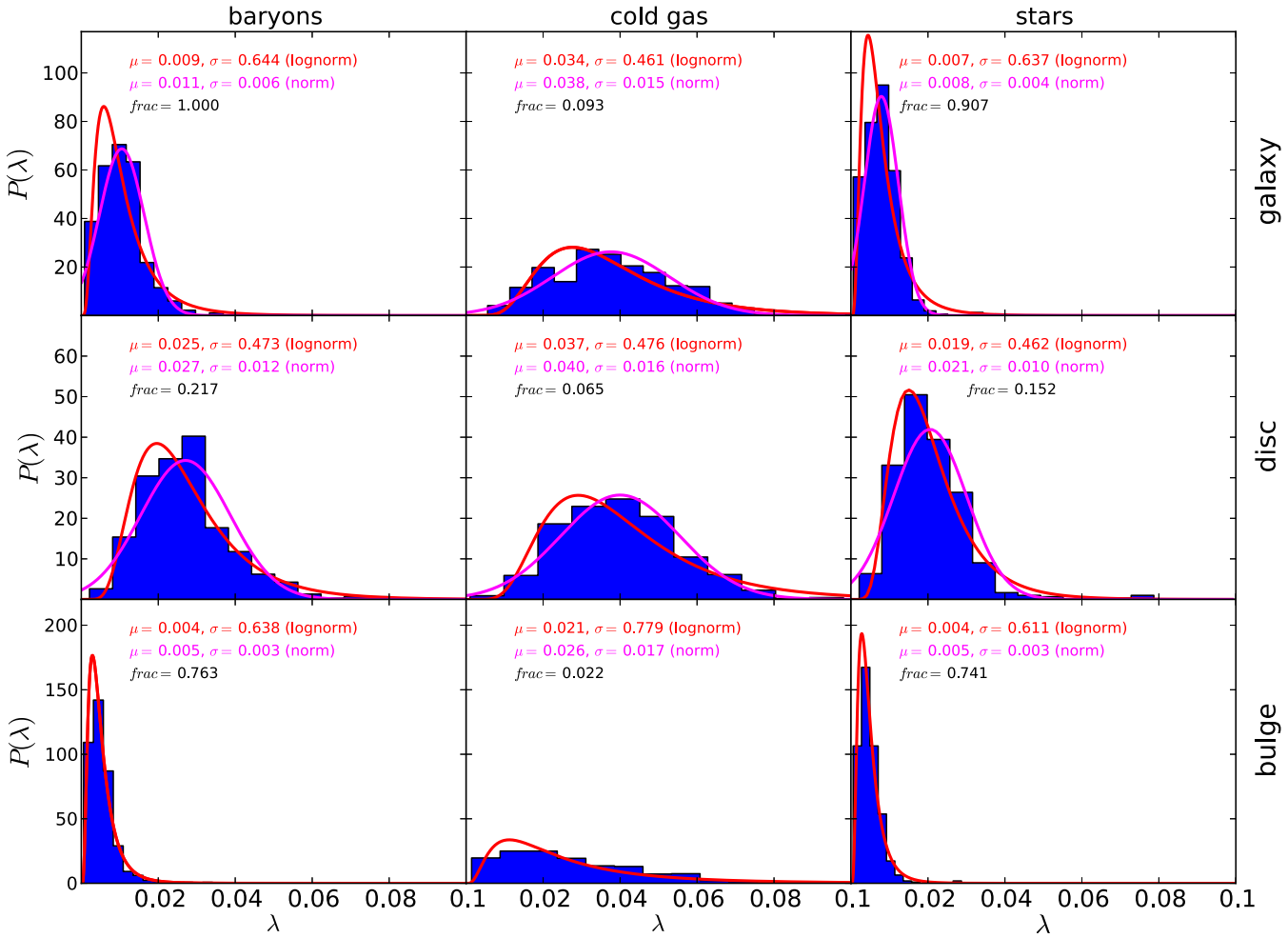

Figure 19. Galaxy spin parameter distributions over all galaxies and snapshots. The columns refer to all the baryons, and divided into cold gas and stars (the hot gas is negligible). The rows refer to the whole galaxy, and divided into disc and bulge. The distributions were fitted by a lognormal (red) and a normal (magenta) distribution, with the quoted mean and standard deviation. The mass fraction in each component is quoted. The disc is confined to a cylinder of radius R_d (Table 1) and height as defined for each galaxy at a given redshift in Mandelker et al. (2014) Only galaxies with a minor-to-major axial ratio smaller than 0.5 are considered. Disc gas and stars are chosen to satisfy the kinematic criterion $j_z \leq 0.8 j_{max}$, while the rest of the stars are assigned to the bulge. The average spin of the baryons in the disc is ∼0.027, only moderately smaller than that of the dark matter in the halo, while the spin of the baryons in the galaxy including the bulge is only ∼0.01. In simulations with stronger feedback, the galaxy spin is typically higher by ∼50 per cent.

the typical gas fraction and SFR at $z \sim 2$ are lower by a factor of ∼2 than the average observed values in star-forming galaxies (Ceverino et al. 2010; Daddi et al. 2010; Tacconi et al. 2010). Furthermore, the simulated mass-loading factor of the galactic outflow rate with respect to the SFR is typically $\eta \lesssim 1$, not reproducing some of the observed strong outflows with mass loading factors of $\eta \gtrsim 1$ (Steidel et al. 2010; Genzel et al. 2011; Dekel & Krumholz 2013). This leads to a stellar-to-halo mass fraction of ∼0.1 within the virial radius, a factor of ∼2–3 higher than the observationally indicated value (e.g. Pérez-González et al. 2008; Behroozi, Wechsler & Conroy 2013; Moster, Naab & White 2013).

We are now in a process of analysing a new suite of galaxies simulated with higher resolution (17.5–30 pc), lower SFR efficiency and stronger stellar feedback including radiative feedback. They are described in accompanying papers (Ceverino et al. 2014a; Moody et al. 2014; Zolotov et al. 2014). The agreement with the gas fraction, SFR and stellar-to-halo mass fraction deduced from observations is significantly better. Preliminary tests of the AM evolution in these simulations indicate that our findings from the current simulations are robust outside the halo and in most of the halo volume. The stronger feedback makes only a small difference in the inner halo, and a somewhat stronger but still small difference in the disc, with no qualitative change. We provide here a brief, preliminary report on these differences, deferring a detailed study of the sensitivity of galaxy AM to feedback strength, including AGN feedback, to future work.

7.2 Robustness to feedback in the halo

Starting with Fig. 1, the spin profiles in the simulations with stronger feedback are similar within ∼10 per cent for all the component at all redshifts, outside the halo, in the outer halo and in the inner halo.

In Fig. 6, which displays the distributions of spin parameters for different components, the simulations with stronger feedback reveal a total baryonic mass in the halo that is lower by ∼35 per cent, while its spin is higher by ∼40 per cent, indicating either more low-spin outflow from the halo or less high-spin inflow into the halo (DeGraf et al., in preparation). The baryonic spins in the volumes $r = (0.1–1)R_v$ and in $r < R_v$ become higher by only 10 per cent and 17 per cent, respectively, indicating that the larger difference in

$r < R_{\rm v}$ is largely due to a higher coherence between the directions of the AM vectors of the different components in the simulations with stronger feedback. In addition, due to the stronger feedback and lower SFR efficiency, the mass fraction of cold gas in the halo is doubled at the expense of stellar fraction in the halo and galaxy. However, the spin of the cold gas in the halo vary by only ∼10 per cent, while the stellar spin becomes lower.

In Fig. 7, showing the evolution of the average spin parameter for different components, the only noticeable effect of stronger feedback seems to be that the spin of cold gas in the halo plus stars in the inner halo becomes larger, by a factor of ∼2. A comparison to the smaller differences seen in Fig. 6 indicates again that this strong effect is largely due to a higher coherence between the directions of the AM vectors of the different components in the simulations with stronger feedback.

Moving to the inner halo, we included in Fig. 11 pictures of two snapshots from the simulations with higher resolution and stronger feedback (two top-left panels). These images demonstrate that the outer ring is a common feature there too. The pictures highlight the tilt of the outer ring, which in one extreme case extends out to beyond 30 kpc (VEL7).

In Fig. 15, which addresses the normalized torque components parallel and perpendicular to the AM, we find that the same general features are revealed by the simulations with stronger feedback. The tendency for lowering the AM amplitude of the outer ring in the inner halo becomes somewhat stronger, possibly due to a somewhat larger extent of the disc.

7.3 Feedback effects in the inner galaxy

Somewhat more noticeable effects of the boosted feedback are limited to the inner galaxy, zone IV. The hot component is negligible there, so the baryons consist of stars and cold gas. In Fig. 6, the stronger feedback is making the baryon spin within $0.1R_{\rm v}$ become higher by ∼10 per cent. However, in Fig. 19, the stronger feedback causes a larger increase of ∼50 per cent inside the disc radius $R_{\rm d}$. One can see in Table 1 that $R_{\rm d}$ is typically smaller than $0.1R_{\rm v}$. This implies that most of the spin increase by feedback is within the disc, inside $R_{\rm d}$, typically at radii of one to a few kpc. This is consistent with low-spin outflows from the central regions. The bulge-to-total stellar mass ratio in the galaxy decreases due to the stronger feedback by about 20 per cent. The changes in the spins of the other components in Fig. 19 are typically less than 20 per cent.

Based on these preliminary comparisons to the simulations with stronger feedback, we conclude that our results concerning the AM-buildup scenario based on the current simulations are qualitatively robust. The spin estimates seem to be accurate to within ∼10 per cent outside and inside the halo, including in the outer ring. On the other hand, the spin of the inner galaxy may be underestimated, by a factor of ∼33 per cent, with the bulge-to-total ratio overestimated by ∼20 per cent.

8 DISCUSSION AND CONCLUSION

The common understanding of AM acquisition by galaxies has been based on the following simplified conjectures (e.g. Fall & Efstathiou 1980; Mo et al. 1998; Bullock et al. 2001). (a) The origin of AM is outside the halo, prior to maximum expansion, and can be understood in terms of TTT. (b) The baryons and the DM initially occupy the same Lagrangian volume and reach a well-defined maximum expansion near which they acquire most of the AM. Therefore, they obtain the same sAM by TTT. (c) In TTT, a second-order expansion of the gravitational potential about the proto-halo centre is sufficient. (d) The gas is heated by a virial shock and it initially shares with the DM the same mass and AM distribution within the halo. (e) The gas feeds the galaxy by wide-angle cylindrical infall and it therefore conserves AM during the infall. (f) The AM of the infalling gas determines the density profile of the disc. Most analytic and semi-analytic modelling of galaxy formation has been based on these conjectures. Here, we addressed the origin of AM in high-redshift galaxies using high-resolution zoom-in cosmological simulations. We analysed the AM evolution in the context of our developing understanding of massive galaxy formation at the nodes of the cosmic web. We found that most of the common simplifying assumptions are actually invalid at high redshift, and that the picture of AM evolution is quite different than originally thought. Nevertheless, at the end of the day, the AM distribution in the final disc is not extremely different from the results of the toy modelling based on the simplified assumptions.

The basic ideas of TTT, and the effective gain of AM prior to maximum expansion in phase I outside the halo, seem to be qualitatively valid. However, the cold gas, confined to elongated pre-contracted thin streams, gains sAM higher than that of the DM by a factor of 1.5–2 because of the high quadrupole moment associated with the thin gas streams while the streams are still near maximum expansion along their major axes. TTT is thus valid but it has to be applied using the inertia tensor of the cold gas after its early contraction to the central cords of the filaments. The DM, on the other hand, streams along much thicker filaments and between them, so, in practice, it accretes from many directions, and thus obeys better the standard TTT applied in Lagrangian space. In phase II in the outer halo, while the DM virializes in the halo and partly mixes with the lower sAM mass that arrived earlier, the cold gas flows in as coherent streams, roughly conserving AM while transporting it to the inner halo, and only there it mixes with the baryons that arrived earlier. As a result, the spin parameter of the cold gas in the halo is ∼3 times larger than that of the DM. In phase III, at the greater disc vicinity in the inner halo, the cold gas settles into an extended non-uniform rotating ring, where torques, partly exerted by the inner disc, make the cold-gas AM decrease in amplitude and align with the inner disc, namely the cold-gas AM is not conserved, and is shared with the rest of the gas, the stars, and the DM. Finally, within the inner disc, outflows increase the effective sAM, and VDI drives AM out and thus makes the density profile more centrally concentrated. This scenario of AM buildup is very different from the common simplified cylindrical infall model.

The encouraging surprise is that the final distribution of spin parameter of the baryons in high-z massive discs is not extremely different from that of the DM in the haloes, both roughly resembling a lognormal distribution with means of $\langle\lambda\rangle \simeq 0.03$ and 0.04, respectively. The stellar disc component has a somewhat lower average spin, $\langle\lambda\rangle \simeq 0.02$, while for the gas component it is somewhat larger, $\langle\lambda\rangle \simeq 0.04$. This implies that the disc sizes predicted by analytic and semi-analytic models are adequate crude approximations with a systematic error smaller than a factor of 2.

Our analysis reveals four phases in the acquisition of AM by the baryons that make high-redshift massive galaxies, as illustrated in Fig. 20. In phase I, well outside the halo, the cold streams gain AM by linear tidal torques from the cosmic web, exerted on the cold gas after its early contraction to the central cords of the filaments feeding the halo. This can also be viewed as asymmetric transverse flows from voids and pancakes into the streams (Pichon et al. 2011). The sAM of the cold gas in narrow streams is higher by a factor of 1.5–2 than that gained by the DM. The AM of the streams is expressed as

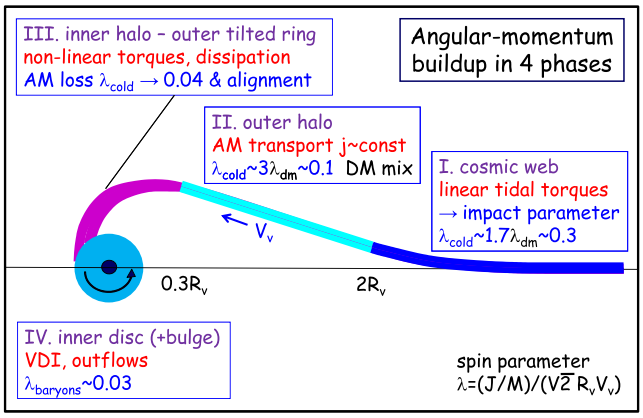

Figure 20. Origin of angular momentum in galaxies fed by cold streams in four steps. Phase I is the linear TTT phase, occurring in the cosmic web outside the halo, where the thin, elongated cold streams acquire more sAM than the dark matter, expressed as impact parameters. Phase II is the transport phase, where the streams flow roughly along straight lines down to $\sim 0.3R_{\rm v}$. Phase III is the strong-torque phase, in a tilted, inflowing, extended ring at $(0.1–0.3)R_{\rm v}$. Phase IV involves the inner disc and the growing bulge, where the final rearrangement of AM occurs due to VDI torques and outflows.

impact parameters with respect to the galaxy centre. The dominant stream typically develops an impact parameter of $\sim 0.3R_{\rm v}$, while the second and third streams have smaller impact parameters, possibly counter-rotating. Phase II involves the coherent transport of cold-gas mass and AM into the halo and through its outer regions. While the DM mixes, the cold streams remain coherent and keep a roughly constant velocity and impact parameter, thus largely preserving AM. The spin parameter of the cold gas in the halo is ~ 3 times larger than that of the DM. The pericentre of the dominant stream dictates the radius of zone III, where the streams dissipate, bend, and settle into an extended ring, a perturbed non-uniform rotating pattern in the greater vicinity of the inner disc.[5] The plane of the outer ring is dictated by the original AM of the dominant stream, which could be tilted with respect to the inner disc (Danovich et al. 2012). Strong torques, largely exerted by the inner disc, cause AM exchange that allows inflow towards the inner disc within less than an orbital time and a gradual alignment with the inner disc. The AM lost from the inspiralling cold gas can go to outflowing gas and to the DM. Finally, there are AM adjustments within the inner disc due to VDI and outflows, which have not been addressed in detail here.

The potential observable properties of the inflowing cold-gas streams through the outer halo have been discussed elsewhere, in absorption (Faucher-Giguère & Kereš 2011; Fumagalli et al. 2011, 2014; Goerdt et al. 2012), and in Lyman α emission (Dijkstra & Loeb 2009; Goerdt et al. 2010). The most practical observable prediction is the existence of an extended rotating ring, extending from ~ 10 to ~ 30 kpc. The extended ring tends to be tilted relative to the inner disc plane, with the tilt increasing with radius, reaching an orientation that is only poorly correlated with the disc orientation.

The internal structure of the extended ring is expected to be filamentary, clumpy, and the gas actually occupies only a fraction of the disc area. About 58 per cent of the lines of sight are of very low H I column densities. However, about 30 per cent of the lines of sight are above a column density of 2×10^{20} H cm^{-2} and are thus observable as damped Lyman α systems. The metallicity of the cold gas in the extended ring is predicted to be about $Z \simeq 0.1$ solar, in the ball park of the observed metallicities in damped Lyman α systems (Fumagalli et al. 2014). These estimates are valid on average for the mass and redshift ranges studied here and for the feedback used, and should therefore be considered as a preliminary proof of concept.

There are preliminary observational indications consistent with an extended ring. Bouché et al. (2013) detected in a $z = 2.3$ galaxy of an estimated virial mass 10^{11} M$_\odot$ a low-metallicity cold-gas absorption system at a projected distance of 26 kpc from the centre, namely about a third of the virial radius, with a radial velocity of 180 km s^{-1} relative to the centre-of-mass velocity, namely consistent with a close-to-circular motion. A detection of low-metallicity CGM gas at 54 kpc from the centre of a $z = 2.4$ galaxy is also reported by Crighton, Hennawi & Prochaska (2013). Observed Mg II absorption lines at large radii in intermediate-redshift galaxies ($z < 1$) indicate velocities consistent with rotation in terms of magnitude and in terms of residing in one side of the galaxy systemic velocity, typically aligned with one arm of the rotation curve (Steidel et al. 2002; Kacprzak et al. 2010).

We found significant counter rotation in the incoming streams of cold gas, at an average level of 75 per cent of its net AM amplitude, which in 15–20 per cent of the cases flips the gas-disc spin in one disc orbital time. This can have important effects on stimulating VDI and triggering a compaction into a 'blue nugget followed by quenching to a 'red nugget' (Zolotov et al. 2014). Disc shrinkage due to counter rotation has been demonstrated in idealized simulations of proto-stellar discs (Dyda et al. 2015).

Counter-rotating stellar components are expected in the disc and its greater environment, reminiscent of the distinct cold streams with opposite impact parameters. Mutually counter-rotating streams tend to dissipate at inner radii and coalesce into one coherently rotating disc, but stars formed prior to this coalescence may end up in mutually counter-rotating discs in the same galaxy. These could dominate at different radii and be tilted relative to each other, or they may reside in the same disc structure. Observational evidence for such counter-rotating discs are reported and discussed (Rubin, Graham & Kenney 1992; Prada & Gutiérrez 1999; Algorry et al. 2013; Corsini 2014, and references therein).

Preliminary comparisons of the results from the current simulations and from a new suite of simulations with higher resolution, lower SFR efficiency and an additional radiative stellar feedback reveal that our main results are robust Section 7. The stronger feedback tends to reduce the bulge-to-disc ratio by ~ 20 per cent and sometimes make the disc more extended, with a spin parameter higher by ~ 50 per cent for the galaxy within the disc radius $R_{\rm d}$, but only by ~ 8 per cent inside $0.1R_{\rm v}$. However, the feedback-driven winds tend to flow perpendicular to the disc and have only weak interaction with the instreaming cold gas (DeGraf et al., in preparation). They therefore have a rather weak effect on the AM of the outer ring in the inner halo, and an even weaker effect on the instreaming cold gas in the halo and outside it. The sensitivity of the galaxy AM to feedback strength, including AGN feedback, is to be addressed in detail in a future study. We note that feedback is likely to have a stronger effect on the AM in less massive galaxies, dwarfs or high-redshift building blocks of massive galaxies (e.g. Dekel & Silk 1986; Maller & Dekel 2002; Governato et al. 2010).

In this work, we have made only limited steps towards a comprehensive study of the presented picture for AM buildup in high-redshift massive galaxies. Future work, analytic and using simulations, should complete the missing details. For example, the

[5] We use the terminology of 'outer tilted ring' in order to distinguish this new feature from the 'inner disc', but the outer ring could sometimes be referred to as an 'outer tilted disc', as the 'ring' spirals in the inner disc and the borders between the zones are not always well defined.

acquisition of AM by linear tidal torques in phase I can be performed in detail, analysing the role played by the cosmic web structure and the pre-collapse of gas into the filament cords. The penetration of the supersonic streams through the outer halo, including the effects of shocks and of hydrodynamical, thermal and gravitational instabilities, would add to the understanding of the transport of mass and AM in this zone. The structure and kinematics of the extended ring in the messy interface region should be investigated in more detail. Finally, the AM-changing processes within the inner disc, including SFR, feedback and VDI, should be addressed more thoroughly with high-resolution simulations that incorporate more realistic feedback.

ACKNOWLEDGEMENTS

We acknowledge stimulating discussions with F. Bournaud, J. Bullock, J. Devriendt, M. Fall, C. Pichon, D. Pogosian, and F. van den Bosch. This research has been supported by ISF grant 24/12, by GIF grant G-1052-104.7/2009, by a DIP grant, by NSF grant AST-1010033, by the I-CORE Program of the PBC and the ISF grant 1829/12. DC is a Juan de la Cierva fellow and he has been partly supported by MINECO grant AYA2012-31101. The simulations were performed in the astro cluster at HU, in the National Energy Research Scientific Computing Center (NERSC) at Lawrence Berkeley National Laboratory, and in NASA Advanced Supercomputing (NAS) at NASA Ames Research Center.

REFERENCES

Agertz O. et al., 2007, MNRAS, 380, 963
Agertz O., Teyssier R., Moore B., 2009, MNRAS, 397, L64
Algorry D. G., Navarro J. F., Abadi M. G., Sales L. V., Steinmetz M., Piontek F., 2013, MNRAS, 437, 3596
Barnes J., Hut P., 1986, Nature, 324, 446
Barro G. et al., 2013, ApJ, 765, 104
Barro G. et al., 2014, preprint (arXiv:1311:0000)
Bauer A., Springel V., 2012, MNRAS, 423, 2558
Behroozi P. S., Wechsler R. H., Conroy C., 2013, ApJ, 762, L31
Bett P., Eke V., Frenk C. S., Jenkins A., Helly J., Navarro J., 2007, MNRAS, 376, 215
Bett P., Eke V., Frenk C. S., Jenkins A., Okamoto T., 2010, MNRAS, 404, 1137
Binney J., 1977, ApJ, 215, 483
Birnboim Y., Dekel A., 2003, MNRAS, 345, 349
Birnboim Y., Dekel A., Neistein E., 2007, MNRAS, 380, 339
Booth C. M., Schaye J., 2009, MNRAS, 398, 53
Bouché N., Murphy M. T., Kacprzak G. G., Péroux C., Contini T., Martin C. L., Dessauges-Zavadsky M., 2013, Science, 341, 50
Bournaud F., Elmegreen B. G., Elmegreen D. M., 2007, ApJ, 670, 237
Bournaud F., Dekel A., Teyssier R., Cacciato M., Daddi E., Juneau S., Shankar F., 2011, ApJ, 741, L33
Brook C. B. et al., 2011, MNRAS, 415, 1051
Brooks A. M. et al., 2011, ApJ, 728, 51
Bullock J. S., Dekel A., Kolatt T. S., Kravtsov A. V., Klypin A. A., Porciani C., Primack J. R., 2001, ApJ, 555, 240
Cattaneo A., Dekel A., Devriendt J., Guiderdoni B., Blaizot J., 2006, MNRAS, 370, 1651
Cattaneo A., Faber S. M., Binney J., Dekel A., Kormendy J., Mushotzky R., 2009, Nature, 460, 213
Ceverino D., Klypin A., 2009, ApJ, 695, 292
Ceverino D., Dekel A., Bournaud F., 2010, MNRAS, 404, 2151
Ceverino D., Dekel A., Mandelker N., Bournaud F., Burkert A., Genzel R., Primack J., 2012, MNRAS, 420, 3490
Ceverino D., Klypin A., Klimek E. S., Trujillo-Gomez S., Churchill C. W., Primack J., Dekel A., 2014a, MNRAS, 442, 1545
Ceverino D., Dekel A., Tweed D., Primack J., 2014b, MNRAS, 447, 3291
Ciotti L., Ostriker J. P., 2007, ApJ, 665, 1038
Codis S., Pichon C., Devriendt J., Slyz A., Pogosyan D., Dubois Y., Sousbie T., 2012, MNRAS, 427, 3320
Corsini E. M., 2014, in Iodice E., Corsini E. M., eds, ASP Conf. Ser. Vol. 486, Multi-Spin Galaxies. Astron. Soc. Pac., San Francisco, p. 51
Crighton N. H. M., Hennawi J. F., Prochaska J. X., 2013, ApJ, 776, L18
Daddi E. et al., 2010, ApJ, 713, 686
Danovich M., Dekel A., Hahn O., Teyssier R., 2012, MNRAS, 422, 1732
DeGraf C., Dekel A., Gabor J., Bournaud F., 2014, preprint (arXiv:1412.3819)
Dekel A., Birnboim Y., 2006, MNRAS, 368, 2
Dekel A., Burkert A., 2014, MNRAS, 438, 1870
Dekel A., Krumholz M. R., 2013, MNRAS, 432, 455
Dekel A., Silk J., 1986, ApJ, 303, 39
Dekel A. et al., 2009, Nature, 457, 451
Dekel A., Sari R., Ceverino D., 2009, ApJ, 703, 785
Dekel A., Zolotov A., Tweed D., Cacciato M., Ceverino D., Primack J. R., 2013, MNRAS, 435, 999
Dijkstra M., Loeb A., 2009, MNRAS, 400, 1109D
Doroshkevich A. G., 1970, Astrophysics, 6, 320
Dutton A. A., van den Bosch2012, MNRAS, 421, 608
Dyda S., Lovelace R. V. E., Ustyugova G. V., Romanova M. M., Koldoba A. V., 2015, MNRAS, 446, 613
Fabian A. C., 2012, ARA&A, 50, 455
Fall S. M., 1983, in Athanassoula E., ed., Proc. IAU Symp. 100, Internal Kinematics and Dynamics of Galaxies. Reidel, Dordrecht, p. 391
Fall S. M., Efstathiou G., 1980, MNRAS, 193, 189
Fall S. M., Romanowsky A. J., 2013, ApJ, 769, L26
Faucher-Giguère C.-A., Kereš D., 2011, MNRAS, 412, L118
Fumagalli M., Prochaska J. X., Kasen D., Dekel A., Ceverino D., Primack J. R., 2011, MNRAS, 418, 1796
Fumagalli M., Hennawi J. F., Prochaska J. X., Kasen D., Dekel A., Ceverino D., Primack J., 2014, ApJ, 780, 74
Fumagalli M., O'Meara J. M., Prochaska J. X., Kanekar N., Wolfe A. M., 2014, MNRAS, 444, 1282
Genzel R. et al., 2006, Nature, 442, 786
Genzel R. et al., 2008, ApJ, 687, 59
Genzel R. et al., 2011, ApJ, 733, 101
Genzel R. et al., 2013, ApJ, 785, 75
Goerdt T., Dekel A., Sternberg A., Ceverino D., Teyssier R., Primack J. R., 2010, MNRAS, 407, 613
Goerdt T., Dekel A., Sternberg A., Gnat O., Ceverino D., 2012, MNRAS, 424, 2292
Governato F. et al., 2010, Nature, 463, 203
Guedes J., Callegari S., Madau P., Mayer L., 2011, ApJ, 742, 76
Hahn O., Teyssier R., Carollo C. M., 2010, MNRAS, 405, 274
Hopkins P. F., Hernquist L., Cox T. J., Robertson B., Springel V., 2006, ApJS, 163, 50
Hopkins P. F., Kereš D., Murray N., Quataert E., Hernquist L., 2012, MNRAS, 427, 968
Hoyle F., 1951, in Burgers J. M., van de Hulst H. C. (eds.), *Problems of Cosmical Aerodynamics*, International Union of Theoretical and Applied Mechanics and IAU, p. 195
Immeli A., Samland M., Westera P., Gerhard O., 2004, ApJ, 611, 20
Kacprzak G. G., Churchill C. W., Ceverino D., Steidel C. C., Klypin A., Murphy M. T., 2010, ApJ, 711, 533
Kennicutt R. C., Jr, 1998, ApJ, 498, 541
Kereš D., Katz N., Weinberg D. H., Davé R., 2005, MNRAS, 363, 2
Kereš D., Katz N., Fardal M., Davé R., Weinberg D. H., 2009, MNRAS, 395, 160
Kimm T., Devriendt J., Slyz A., Pichon C., Kassin S. A., Dubois Y., 2011, preprint (arXiv:1106.0538)
Komatsu E. et al., 2009, ApJS, 180, 330
Kravtsov A. V., 2003, ApJ, 590, L1
Kravtsov A. V., Klypin A. A., Khokhlov A. M., 1997, ApJS, 111, 73
Krumholz M. R., Dekel A., 2010, MNRAS, 406, 112
Krumholz M. R., Dekel A., 2012, ApJ, 753, 16

Maller A. H., Dekel A., 2002, MNRAS, 335, 487
Maller A. H., Dekel A., Somerville R., 2002, MNRAS, 329, 423
Mandelker N., Dekel A., Ceverino D., Tweed D., Moody C. E., Primack J., 2014, MNRAS, 443, 3675
Mo H. J., Mao S., White S. D. M., 1998, MNRAS, 295, 319
Moody C. E., Guo Y., Mandelker N., Ceverino D., Mozena M., Koo D. C., Dekel A., Primack J., 2014, MNRAS, 444, 1389
Moster B. P., Naab T., White S. D. M., 2013, MNRAS, 428, 3121
Murray N., Quataert E., Thompson T. A., 2010, ApJ, 709, 191
Navarro J. F., Abadi M. G., Steinmetz M., 2004, ApJ, 613, L41
Nelson D., Vogelsberger M., Genel S., Sijacki D., Kereš D., Springel V., Hernquist L., 2013, MNRAS, 429, 3353
Noguchi M., 1999, ApJ, 514, 77
Ocvirk P., Pichon C., Teyssier R., 2008, MNRAS, 390, 1326
Peebles P. J. E., 1969, ApJ, 155, 393
Pérez-González P. G. et al., 2008, ApJ, 675, 234
Pichon C., Pogosyan D., Kimm T., Slyz A., Devriendt J., Dubois Y., 2011, MNRAS, 418, 2493
Porciani C., Dekel A., Hoffman Y., 2002a, MNRAS, 332, 325
Porciani C., Dekel A., Hoffman Y., 2002b, MNRAS, 332, 339
Powell L. C., Slyz A., Devriendt J., 2011, MNRAS, 414, 3671
Prada F., Gutiérrez C. M., 1999, ApJ, 517, 123
Prada F., Klypin A. A., Simonneau E., Betancort-Rijo J., Patiri S., Gottlöber S., Sanchez-Conde M. A., 2006, ApJ, 645, 1001
Rees M. J., Ostriker J. P., 1977, MNRAS, 179, 541
Romanowsky A. J., Fall S. M., 2012, ApJS, 203, 17
Rubin V. C., Graham J. A., Kenney J. D. P., 1992, ApJ, 394, L9
Scannapieco C. et al., 2012, MNRAS, 423, 1726
Sharma S., Steinmetz M., 2005, ApJ, 628, 21
Silk J., 1977, ApJ, 211, 638
Silk J., Rees M. J., 1998, A&A, 331, L1
Steidel C. C., Kollmeier J. A., Shapley A. E., Churchill C. W., Dickinson M., Pettini M., 2002, ApJ, 570, 526
Steidel C. C., Erb D. K., Shapley A. E., Pettini M., Reddy N., Bogosavljević M., Rudie G. C., Rakic O., 2010, ApJ, 717, 289
Stewart K. R., Kaufmann T., Bullock J. S., Barton E. J., Maller A. H., Diemand J., Wadsley J., 2011, ApJ, 738, 39
Stewart K. R., Brooks A. M., Bullock J. S., Maller A. H., Diemand J., Wadsley J., Moustakas L. A., 2013, ApJ, 769, 74
Tacconi L. J. et al., 2010, Nature, 463, 781
Tillson H., Devriendt J., Slyz A., Miller L., Pichon C., 2012, preprint (arXiv:1211.3124)
White S. D. M., 1984, ApJ, 286, 38
Zolotov A., Dekel A., Mandelker N., Tweed D., Inoue S., DeGraf C., Ceverino D., Primack J., 2014, preprint (arXiv:1412.4783)

This paper has been typeset from a TEX/LATEX file prepared by the author.